



ChemComm

**Mixed Oxides as Multi-Functional Reaction Media for  
Chemical Looping Catalysis**

|               |                          |
|---------------|--------------------------|
| Journal:      | <i>ChemComm</i>          |
| Manuscript ID | CC-FEA-10-2022-005502.R1 |
| Article Type: | Feature Article          |
|               |                          |

SCHOLARONE™  
Manuscripts

# Mixed Oxides as Multi-Functional Reaction Media for Chemical Looping Catalysis

Junchen Liu<sup>1</sup>, Fanxing Li<sup>1\*</sup>

<sup>1</sup> *Chemical and Biomolecular Engineering, North Carolina State University, Raleigh, NC, USA*

*\*Corresponding Author, fli5@ncsu.edu,*

**Abstract** – Over the past two decades, chemical looping combustion (CLC) has been extensively investigated as a promising means to produce electric power while generating a concentrated carbon dioxide stream for sequestration. We note that the chemical looping strategy can be extended well outside of combustion-based carbon capture. In fact, application of the chemical looping strategy in areas beyond combustion can result in somewhat unexpected energy and carbon dioxide savings without producing a concentrated CO<sub>2</sub> stream at all. Furthermore, it allows the looping-based technologies to tap into applications such as chemical production – a \$4 trillion/year industrial sector with high energy and carbon intensities. The key resides in the design of effective oxygen carriers, also known as redox catalysts in the context of selective chemical conversion through chemical looping catalysis (CLCa). This contribution focuses on the design and applications of mixed oxides as multi-function reaction media in CLCa. Since typical mixed oxide oxygen carriers tend to be nonselective for hydrocarbon conversion, the first part of this article presents generalized design principles for surface modification of mixed oxides to improve their selectivity and catalytic activity. Applications of these redox catalysts in chemical looping – oxidative dehydrogenation (CL-ODH) of a variety of light alkanes and alkyl-benzenes are presented. This is followed with a discussion of computation assisted mixed oxide design based upon thermodynamic criteria. Finally, a few new directions for the chemical looping technologies are introduced.

## 1 Introduction

The chemical industry contributes to nearly 1 gigaton of direct CO<sub>2</sub> emission each year.<sup>1</sup> In addition, nearly 50% of the oil and natural gas input in the chemical sector is consumed as the feedstock, which can lead to secondary emissions in the downstream industrial and/or consumer sectors.<sup>1</sup> Despite the projected strong growth, the chemical industry is expected to curb its emission within this decade according to the Net Zero by 2050 roadmap proposed by the International Energy Agency (IEA).<sup>2</sup> In fact, several leading chemical and petrochemical companies have pledged more aggressive emission reduction targets over the recent years. However, not surprisingly, CO<sub>2</sub> emissions from state-of-the-art chemical production processes tie directly to the energy intensity of the manufacturing process as well as the annual production capacity. **Figure 1a** summarizes the production capacity and emission levels from a few key commodity chemicals. Although the overall CO<sub>2</sub> emissions can be reduced, to some extent, by switching to low carbon intensity fuels and increasing the renewable contribution to the electrical grid, such incremental improvements to the existing technologies are unlikely to attain the net zero target by 2050. Rather, transformative chemical production technologies that are fundamentally different from state-of-the-art approaches are required.

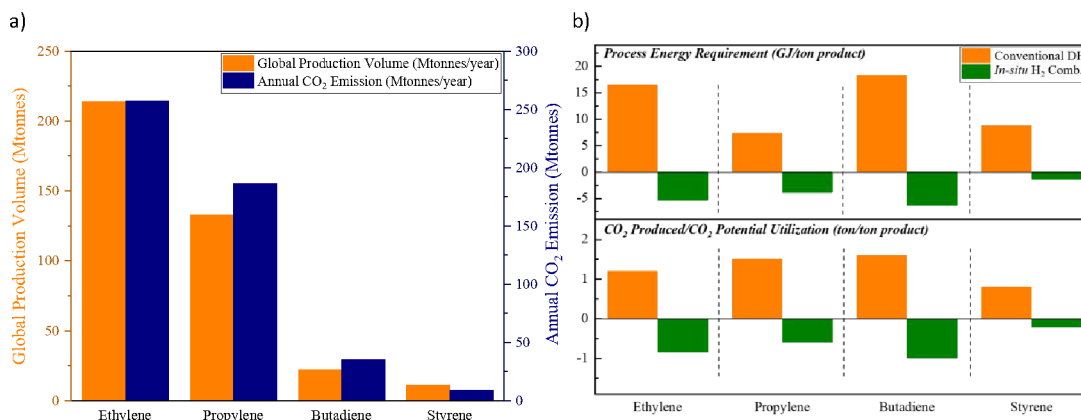
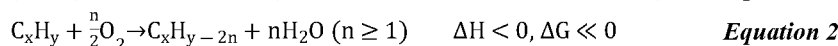
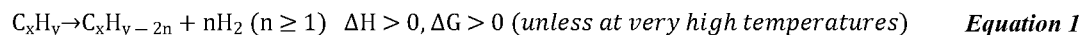


**Figure 1.** a) The global annual production volumes and the associated CO<sub>2</sub> emissions of ethylene, propylene, butadiene, and styrene<sup>3-10</sup>; b) **Top:** Comparison between the energy requirement of conventional dehydrogenation (DH) processes to that of the oxidative processes with *in-situ* H<sub>2</sub> combustion (assuming an ideal process with 100% hydrogen byproduct combustion); **Bottom:** Comparison between the CO<sub>2</sub> emission from the existing processes to the CO<sub>2</sub> utilization potential from the energy resulting from *in-situ* H<sub>2</sub> combustion (assuming an ideal scenario of utilizing the energy from H<sub>2</sub> combustion for CO<sub>2</sub> splitting to CO)<sup>3-10</sup>.

At present, the unsaturated hydrocarbons (i.e. Ethylene<sup>3</sup>, Propylene<sup>4-8</sup>, Butadiene<sup>3, 7</sup> and Styrene<sup>9, 10</sup>) listed in **Figure 1** are primarily produced by dehydrogenation or cracking processes, either thermally or in the presence of a heterogeneous catalyst. Common limitations for such processes include large heat requirement and equilibrium-limited single-pass yield due to the highly endothermic and endergonic nature of the reactions, shown in **Equation 1**. The limited product yield and selectivity in turn drive up the energy consumption and CO<sub>2</sub> emissions associated with product separation.



It has long been recognized that (catalytic) oxidative conversion of the same feed molecules in the presence of gaseous oxygen would address the aforementioned limitations by changing the highly endothermic reactions into highly exothermic ones (**Figure 1b**). The exergonic nature of H<sub>2</sub> oxidation also eliminates the equilibrium limitations, shown with **Equation 2**. Despite these advantages, commercial adoption of oxidative cracking (OC) or oxidative dehydrogenation (ODH) technologies have been scarce. In addition to the limited catalytic selectivity and stability, the key obstacles hindering the development of ODH technologies resides in the safety concerns over co-feeding oxygen with hydrocarbon feedstocks and the high cost and energy consumptions for oxygen generation. In fact, state-of-the-art cryogenic air separation technology itself only achieves a 25% second law efficiency, or ~0.78 GJ/tonne O<sub>2</sub> in terms of actual energy consumption<sup>11, 12</sup>, making it a highly energy and emission intensive industrial process.

Resulting from three decades of research, a wealth of knowledge has been created for the chemical looping technology in terms of the oxygen carrier selection and performance, reactor design and operation, and the overall technological feasibility, primarily in the context of CO<sub>2</sub> capture from fossil fuel combustion via chemical looping combustion (CLC).<sup>13-51</sup> Shown in

Figure 2a, CLC technologies generally involves two cyclic steps: (1) the use of metal oxide(s) oxygen carrier as the oxidant to fully combust fossil fuels such as coal or methane; (2) the regeneration of the reduced metal oxide(s) in step 1 with air. We note that the core ideas of the CLC strategy reside in *in-situ* oxygen separation from the air and indirect oxidation of carbonaceous fuels. Therefore, the use of chemical looping for efficient air separation (CLAS) represents a natural extension of CLC, as explored by many chemical looping researchers.<sup>52-94</sup> Furthermore, marrying the chemical looping strategy with oxidative catalysis offers a unique opportunity to intensify the production of a few important commodity chemicals with substantially decreased energy consumption and CO<sub>2</sub> emissions.<sup>95-136</sup> Given that separation processes consume ~60% of the total energy usage in chemical and petroleum industries and heterogeneous catalysts are responsible for >80% of all chemical products worldwide, chemical looping catalysis (CLCa) in this article, has the potential to facilitate process intensification throughout the chemical manufacturing sector by combining catalytic reactions with separations.<sup>120, 137-142</sup> The abovementioned chemical looping process types are summarized in Table 1. In the context of CLCa, the oxygen carriers are denoted as *redox catalysts* to capture their dual functionality.

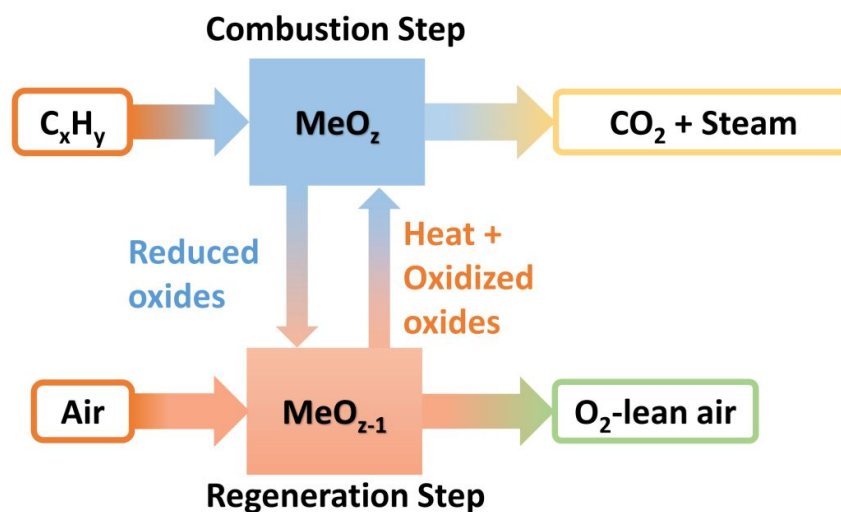
**Table 1.** Generalized chemical looping reactions by process type (the reactions are not balanced. ODH was used as a CLCa example for illustration purpose).

| Process Type | Reactions   |
|--------------|---|
| CLC          | $\text{Fuels} + \text{MeO}_x \rightarrow \text{CO}_2 + \text{H}_2\text{O} + \text{MeO}_{x-\delta}$ $\text{Air} + \text{MeO}_{x-\delta} \rightarrow \text{MeO}_x + \text{N}_2$                         |
| CLAS         | $\text{MeO}_x \rightarrow \text{O}_2 + \text{MeO}_{x-\delta}$ $\text{Air} + \text{MeO}_{x-\delta} \rightarrow \text{MeO}_x + \text{N}_2$  |
| CLCa         | $\text{C}_x\text{H}_y + \text{MeO}_x \rightarrow \text{C}_x\text{H}_{y-2n} + 2n\text{H}_2\text{O} + \text{MeO}_{x-\delta}$ $\text{Air} + \text{MeO}_{x-\delta} \rightarrow \text{MeO}_x + \text{N}_2$ |

Taking ethane ODH as an example, the redox catalyst particles first convert ethane into ethylene and water using its active lattice oxygen. After completing this ODH step, the oxygen-depleted redox catalyst is exposed to air (and/or steam), to replenish the lattice oxygen<sup>143</sup>. Compared to conventional co-feed type ODH reactions, chemical looping process could partition the gaseous oxidant and the hydrocarbons, decreasing the selectivities towards unwanted CO<sub>x</sub> and oxygenated. This CLCa process can be carried out either in circulating fluidized beds similar to a CFB combustor or parallel packed beds operated similar to the Houdry process<sup>3, 137, 144</sup>. The advantages of the redox catalysts and CLCa compared to conventional, heterogeneous ODH catalysts include: (i) integration of catalytic reaction with air separation (a simpler and safer process); (ii) potential to achieve high selectivity (absence of gaseous oxygen inhibits side reactions); (iii) potential to tailor heat of reactions, by varying the metal oxide's redox properties, for improved heat management in the redox steps.<sup>137, 145</sup> Our recent studies indicated that up to 84% energy savings and emission reductions can be realized by CLCa.<sup>137</sup> **Figure 2** illustrates a generalized schematic for CLCa in the context of oxidative dehydrogenation of hydrocarbons.

As will be discussed in the following sections, the potential of chemical looping extends well beyond oxidation catalysis.

a)



b)

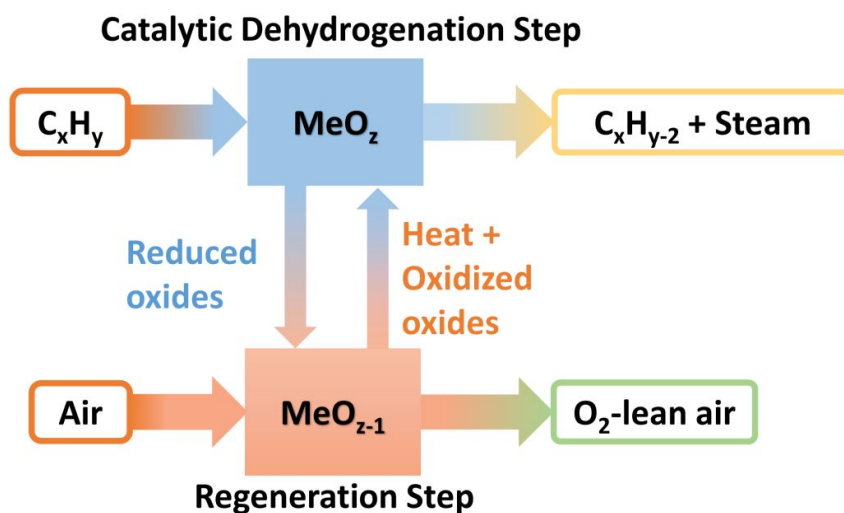


**Figure 2.** Schematic illustration of: a) a generic CLC process: A metal oxide redox catalyst combusts fuel into  $\text{CO}_2$  in the oxidation step; The reduced metal oxide is reoxidized in the regeneration step with air; b) A metal oxide redox catalyst oxidatively converts a light alkane into an olefin product in the oxidation step; The reduced metal oxide is reoxidized in the regeneration step with air.

## 2 Redox Catalyst Design in CLCa for Olefin Production

Complete oxidation of carbonaceous fuels (to  $\text{CO}_2$  and  $\text{H}_2\text{O}$ ) is expected for CLC because this will maximize the heat release, increase the power generation efficiency, and produce a near “sequestration ready”  $\text{CO}_2$  stream<sup>46</sup>. In contrast, CLCa needs to avoid full oxidation since the target products would be value-add fuels and chemicals such as  $\text{H}_2$ ,  $\text{CO}$ , or unsaturated organic molecules. With such expectations, typical CLC oxides alone would not be effective for CLCa because they tend to result in poor product selectivity. This is not at all surprising given that typical CLC oxygen carriers, particularly those composed of mixed oxides, are often specifically designed to have high equilibrium oxygen chemical potential ( $\mu_{\text{O}_2}$ ), facile oxygen evolution kinetics, and (in many cases) highly basic surfaces<sup>121, 146-149</sup>. Therefore, the most critical aspect for CLCa resides in selectivity enhancement of redox-active metal oxides. Given

that the (non-selective) reactions occur at the gas-oxide interfaces, surface modification of the oxides is almost always necessary in order to enhance the product selectivity.

Addition of dopants and/or modulating the metal-oxygen bonding strength on the surface have been shown to be effective to enhance the selectivity towards light olefins for a number of redox oxides and reactions<sup>106, 150</sup>. This section focuses on presenting a more “generalized strategy” for surface modification of mixed oxide in the context of oxidative dehydrogenation of hydrocarbons: instead of doping or impregnation of small amount of heteroatoms on the surface, we reasoned that complete or near-complete coverage of a non-selective oxide surface with a catalytically active layer would effectively suppress side reactions. This approach was first validated in our group for methane partial oxidation reactions<sup>122, 151, 152</sup>, and was recently extended to a series of ODH reactions using various core and shell materials, as illustrated in **Figure 3**<sup>119-121, 138, 143, 144, 147, 153-161</sup>. We categorize this generalized ODH strategy into three types: **Type 1**, shown in **Figure 3a**, involves covering the non-selective mixed oxides with an “inert” molten salt layer to simply block the non-selective sites on the surface, thereby inhibiting nonselective oxidation. In this case, the redox catalyst primarily functions as an oxygen carrying agent for selective hydrogen combustion (SHC); **Type 2**, as illustrated in **Figure 3b**, utilizes an “active” molten salt as the surface layer. With the assistance of the oxygen species supplied from the mixed oxide, this active surface layer can accommodate and/or generate active oxidants, e.g. electrophilic oxygen species or halogen atoms, to initiate C-H bond activation at the gas-molten salt interface. The reactions likely proceed through a surface-initiated gas phase radical reaction pathway, with concurrent hydrogen oxidation; **Type 3**, shown in **Figure 3c**, involves covering the oxide substrate with a solid catalytic shell to catalyze the dehydrogenation reactions, and the H<sub>2</sub> byproduct is sequentially combusted by the oxygen supplied by the oxide core. The following sections further elaborate on these core-shell redox catalyst design strategies.

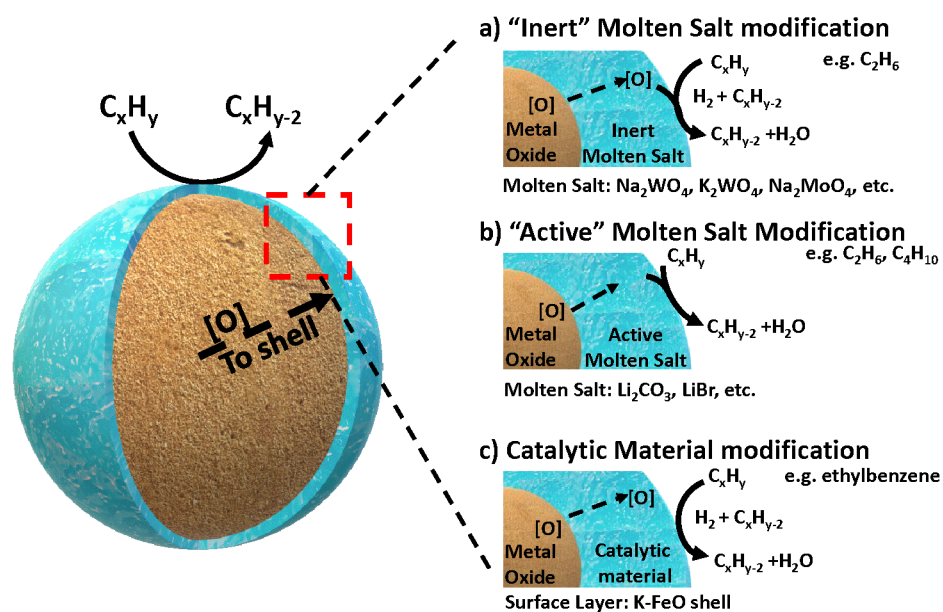


**Figure 3.** General core-shell design frameworks for mixed oxide@molten salt catalysts and mixed oxide@catalytic shell catalysts: a) Type 1: “Inert” molten salt promoted mixed oxides; b) Type 2: “Active” molten salt promoted mixed oxide; c) Type 3: Catalytic material promoted mixed oxides. [O] stands for the

oxygen species donated from the oxide surface, which is responsible for the oxidation reaction. Details of the various oxygen species and their evolution are discussed in Section 2.1.

## 2.1 Mixed oxide @ molten salt redox catalyst for light alkane conversion

### 2.1.1 Type 1: “Inert” molten salt modification

A **Type 1** redox catalyst functions primarily as an oxygen separation and donation agent for selective hydrogen combustion. Therefore, the formation of unsaturated hydrocarbon products would rely on a separate reaction pathway such as thermal cracking or catalytic dehydrogenation. In this case, selectively combusting the hydrogen byproduct would eliminate the equilibrium limitations and supply the heat required by the endothermic dehydrogenation or cracking reactions. A typical application of **Type 1** redox catalysts is ethylene production via thermal cracking of ethane. In this context, we developed redox catalysts based on selected molten salt and Mn-based oxides, e.g.  $\text{Mg}_6\text{MnO}_8$ <sup>121, 147</sup>,  $(\text{Fe}/\text{Mn})\text{O}_x$ <sup>153</sup>,  $(\text{Mn}/\text{Si})\text{O}_x$ <sup>154</sup>, and  $\text{CaMnO}_{3.8}$ <sup>144, 158</sup>, with tungstates, vanadates and/or molybdates molten salts.<sup>147, 162, 163</sup>

Among these redox catalysts,  $\text{Mg}_6\text{MnO}_8@Na_2WO_4$  was the most thoroughly studied.<sup>121, 147</sup> As shown in the **Figure 4a**, co-impregnating Na and W at any ratios on  $\text{Mg}_6\text{MnO}_8$  would lead to significant increase in olefin selectivity and yield.<sup>147</sup> Of the various Na:W ratio investigated, the  $\text{Mg}_6\text{MnO}_8@Na_2WO_4$  (Na:W=2:1) redox catalyst exhibited one of the highest increase in  $\text{C}_2\text{H}_4$  yield (~45% increase, on an absolute scale) compared to the unpromoted  $\text{Mg}_6\text{MnO}_8$  at 850 °C and 4500 hr<sup>-1</sup>. The yield increase was primarily resulted from the substantially decreased  $\text{CO}_x$  selectivity (>80%).  $\text{Mg}_6\text{MnO}_8@Na_2WO_4$  also exhibited well defined crystalline phases at room temperature ( $\text{Mg}_6\text{MnO}_8$  and  $\text{Na}_2\text{WO}_4$ ), with only a minor  $\text{Na}_4\text{Mg}(\text{WO}_4)_3$  phase (**Figure 4b**). The core-shell structure of the catalyst was verified by low-energy ion scattering spectroscopy (LEIS) (**Figure 4c**) and X-ray photoelectron spectroscopy (XPS) (**Figure 4d**)<sup>121</sup>. Even after 10 cycles of sputtering, W and Na/Mg are still far more prevalent than Mn according to LEIS. It is noted that LEIS cannot accurately differentiate Na and Mg due to their similar atomic weights. XPS, which provides near surface elemental compositions (**Figure 4c**), also confirmed the suppression of Mn by  $\text{Na}_2\text{WO}_4$ . In fact, impregnation of  $\text{Na}_2\text{WO}_4$  onto many Mn-containing oxides has shown to create an oxide@  $\text{Na}_2\text{WO}_4$  core shell structure. For instance, transmission electron microscope with energy dispersive x-ray spectroscopy (TEM-EDS) images published from our group by Hao et al. indicated a core shell structure of  $\text{CaMn}_{0.75}\text{Fe}_{0.25}\text{O}_3(\text{CMFO})@Na_2WO_4$  (**Figure 4e**)<sup>157</sup> whereas LEIS and/or XPS data indicated surface enrichment of  $\text{Na}_2\text{WO}_4$  on mixed  $(\text{Fe}/\text{Mn})\text{O}_x$ <sup>153</sup>,  $(\text{Mn}/\text{Si})\text{O}_x$ <sup>154</sup>,  $(\text{Mn}/\text{Cu})\text{O}_x$ <sup>118, 164</sup>, and a number of perovskite oxides. The formation of core-shell structure is likely to be due to the relatively low melting point of  $\text{Na}_2\text{WO}_4$  (698 °C)<sup>165</sup> and low surface tension of the molten salt on typical oxide surfaces.

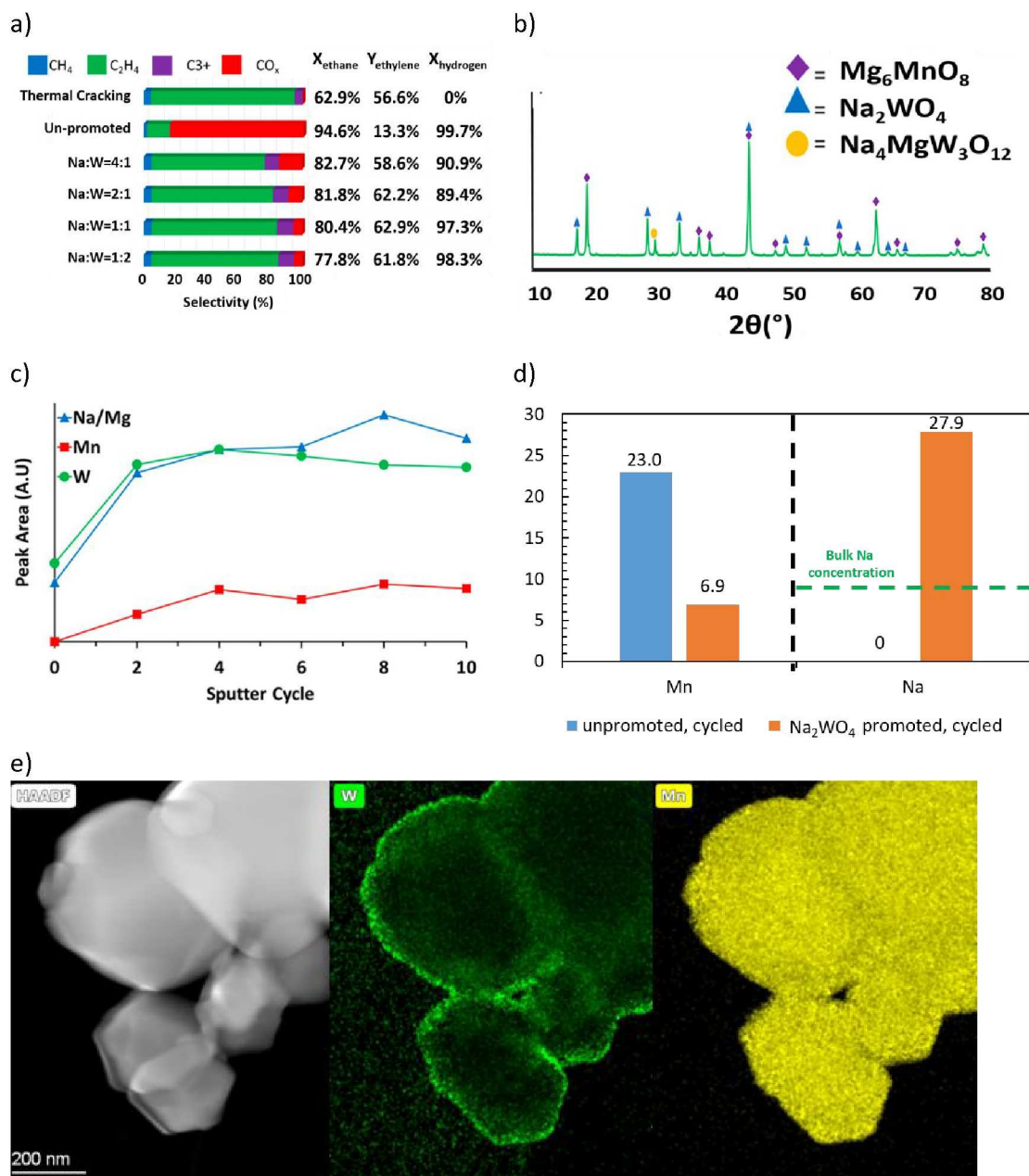


**Figure 4.** a) Performance data of the CL-ODH with Na, W promoted  $\text{Mg}_6\text{MnO}_8$  at  $850\text{ }^\circ\text{C}$  and  $\text{GHSV} = 4500\text{ h}^{-1}$ ; b) X-ray diffraction characterization of  $\text{Mg}_6\text{MnO}_8@Na_2WO_4$ ; c) LEIS peak area over sputter cycles for  $\text{Mg}_6\text{MnO}_8@Na_2WO_4$ ; d) XPS near surface concentration of Na and W of the cycled sample; e) TEM-EDS of  $\text{Mg}_6\text{MnO}_8@Na_2WO_4$

Detailed mechanistic studies from our group were conducted by Yusuf et al. to understand the function and mechanism of the molten salt promoter for **Type 1** redox catalyst<sup>121, 147</sup>.  $\text{Mg}_6\text{MnO}_8@Na_2WO_4$  was used as the model catalyst. Methanol TPSR experiment (**Figure 5a**) showed that the presence of  $Na_2WO_4$  led to significantly decreased  $CO_2$  signal. This suggests that  $Na_2WO_4$  would suppress the basic sites on the surface of  $\text{Mg}_6\text{MnO}_8$ <sup>121</sup>. Mn  $2p_{3/2}$  region scan from XPS **Figure 5b** showed that the high peaks corresponding to  $Mn^{4+}$  at 644.1 eV and 641.7 eV were suppressed in  $\text{Mg}_6\text{MnO}_8@Na_2WO_4$  as compared to the unpromoted  $\text{Mg}_6\text{MnO}_8$ <sup>121</sup>. This corresponds well to the decrease in the basic sites on the surface. Oxygen donation/reincorporation dynamics were also probed with  $^{18}O/^{16}O$  isotope exchange

experiments, shown in **Figure 5c** and **Table 2**<sup>121</sup>. The presence of molten  $\text{Na}_2\text{WO}_4$  inhibits oxygen exchange, particularly in terms of limiting the incorporation rates of dissociatively adsorbed oxygen into the  $\text{Na}_2\text{WO}_4$  layer. Gas switching experiments between  $\text{H}_2$  and  $\text{O}_2$  further indicated that  $\text{H}_2$  solubility in  $\text{Na}_2\text{WO}_4$  was negligible, thus indicating that the hydrogen combustion reaction would occur on the molten salt – gas interface. Therefore, it can be inferred that  $\text{Na}_2\text{WO}_4$  decreases the  $\text{CO}_x$  formation by increasing the energy barrier for the release of the active lattice oxygen at the reaction interface. Electrochemical impedance spectroscopy (EIS) measurements confirmed that oxygen and electron can transport within the  $\text{Na}_2\text{WO}_4$  molten layer to facilitate selective  $\text{H}_2$  combustion (**Figure 5d**)<sup>158</sup>. It was further shown that  $\text{Na}_2\text{WO}_4$  was redox active between  $\text{W}^{6+}$  and  $\text{W}^{5+}$  even though the bulk  $\text{Na}_2\text{WO}_4$  phase was difficult to be fully reduced. As such,  $\text{WO}_4^{2-}/\text{WO}_3^-$  redox pair would act as the intermediate to shuttle oxygen to and from the  $\text{Na}_2\text{WO}_4$  core for selective hydrogen combustion following the following mechanism (**Figure 5e**):

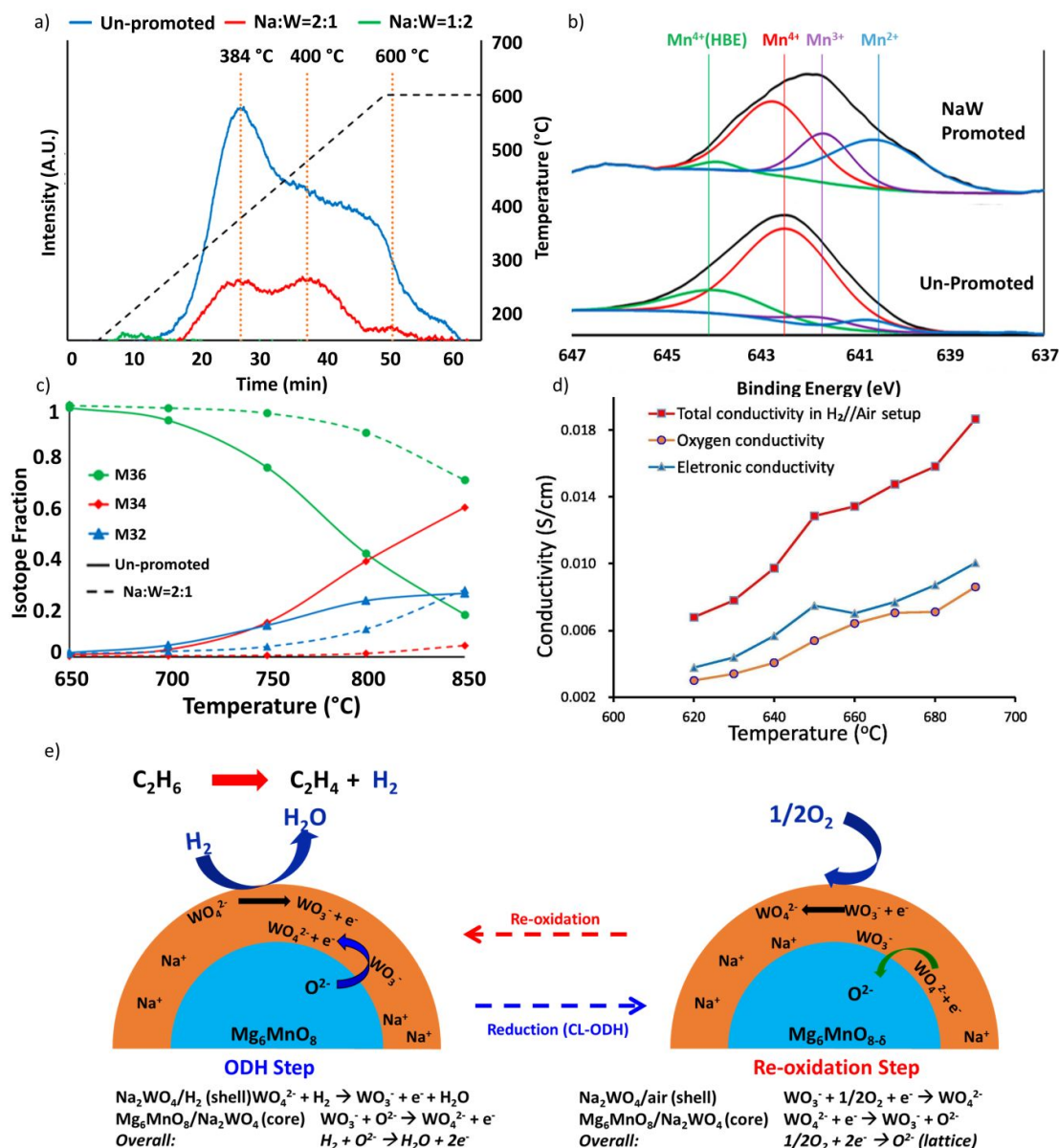


**Figure 5.** a) CO<sub>2</sub> signal Methanol TPSR of Mg<sub>6</sub>MnO<sub>8</sub> and Mg<sub>6</sub>MnO<sub>8</sub>@Na<sub>2</sub>WO<sub>4</sub><sup>121</sup>; b) XPS spectra of manganese 2p<sub>3/2</sub> peaks of cycled redox catalysts<sup>147</sup>; c) <sup>18</sup>O-<sup>16</sup>O isotope exchange experiment<sup>121</sup>; d) Oxygen ion conductivity and electronic conductivity of Na<sub>2</sub>WO<sub>4</sub><sup>158</sup>; e) Proposed mechanism of Mg<sub>6</sub>MnO<sub>8</sub>@Na<sub>2</sub>WO<sub>4</sub><sup>121</sup>

**Table 2.** Arrhenius Activation Energies for Mg<sub>6</sub>MnO<sub>8</sub> and Mg<sub>6</sub>MnO<sub>8</sub>@Na<sub>2</sub>WO<sub>4</sub><sup>121</sup>

| Activation Energy | Mg <sub>6</sub> MnO <sub>8</sub> (kJ/mol) | Mg <sub>6</sub> MnO <sub>8</sub> @Na <sub>2</sub> WO <sub>4</sub> (kJ/mol) (800–850 °C) |
|-------------------|---|---|
| E <sub>Ro</sub>   | 163.83                                    | 202.58  |
| E <sub>Ra</sub>   | 227.18                                    | 205.04  |
| E <sub>Ri</sub>   | 123.82                                    | 174.68  |

R<sub>o</sub>: Overall oxygen exchange rate;  
R<sub>a</sub>: Dissociative oxygen adsorption rate;  
R<sub>i</sub>: Adsorbed oxygen incorporation rate

The same strategy can be extended to many other Mn based oxides and molten salts<sup>153, 154, 157, 158, 164</sup>. In a recent study, we demonstrated this strategy with Mg<sub>6</sub>MnO<sub>8</sub> and (Cu/Mn)O<sub>x</sub> as the redox core and W, V, Mo based alkali salts as the surface promoters<sup>164</sup>. All the abovementioned molten salts were shown to be effective to decrease the CO<sub>x</sub> selectivities from >90%

(unpromoted oxides) to <15% (**Figure 6a and b**) at 850 °C. C<sub>2</sub>H<sub>4</sub> selectivities were maintained >80% while achieving up to ~90% H<sub>2</sub> conversion. As shown in **Figure 6a**, up to ~74% C<sub>2</sub>H<sub>4</sub> yield at 80 vol. % C<sub>2</sub>H<sub>6</sub> feed and 850 °C can be achieved. **Figure 6a** also demonstrated the effect of different molten promoters. The use of multiple alkali metal cations (e.g. Li and Na) and/or transition metals for the salt anion (e.g. Mo and W) were shown to improve the redox catalyst performance in several cases. Such combinative effect further increases the flexibility for designing the **Type 1** catalyst.

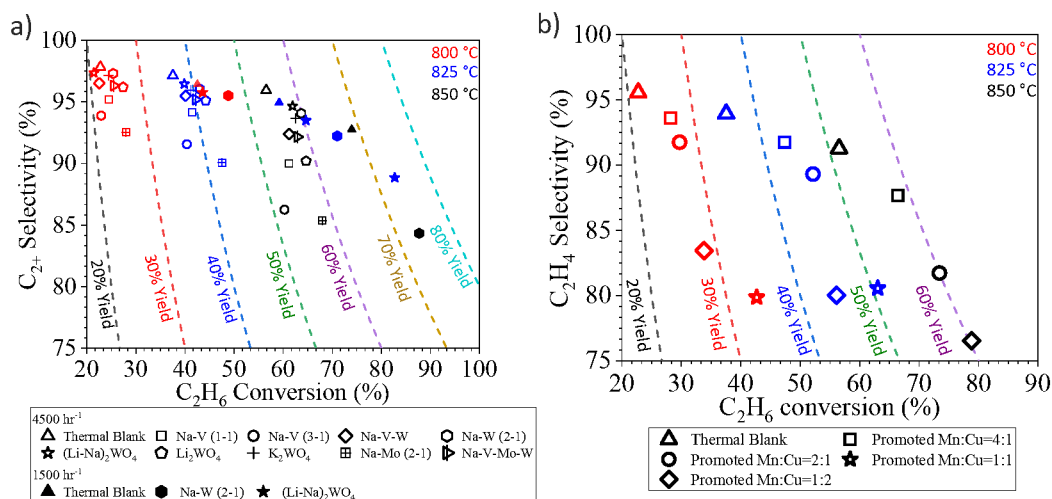


**Figure 6.** a) Performance data of the CL-ODH with alkali W, V, Mo molten salt shell and Mg<sub>6</sub>MnO<sub>8</sub> core at 850 °C at 4500 hr<sup>-1</sup>.<sup>164</sup> b) Performance data of the CL-ODH with Na<sub>2</sub>WO<sub>4</sub> molten salt shell and Cu/MnO<sub>x</sub> core at 850 °C at 4500 hr<sup>-1</sup>.<sup>164</sup>

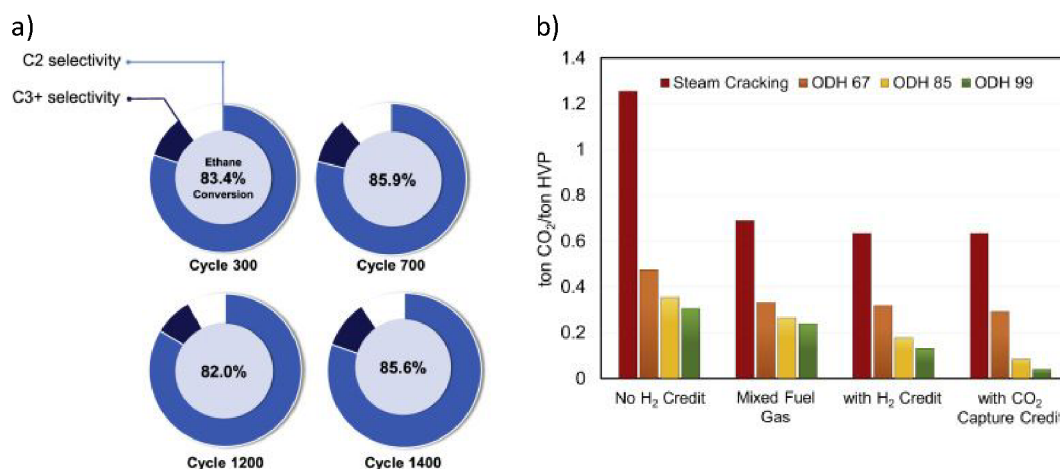


**Figure 7.** a) C<sub>2</sub>H<sub>6</sub> conversion and selectivity profile of the prototype redox catalyst over 1400 cycles at 845 °C, 15–30 mol. % ethane and GHSV=2000 hr<sup>-1</sup> – 3250 hr<sup>-1</sup>; b) CO<sub>2</sub> Emissions of Steam Cracking and ODH Processes under different scenarios For ODH 67/85/99, the numerical value indicates the ethane conversion value in percentage.<sup>129</sup>

Catalyst stability was also demonstrated through a long-term study using a more mechanically robust prototype redox catalyst designed based on the aforementioned principles<sup>129</sup>. As shown in **Figure 7a**, stable product selectivity and ethane conversion were maintained, throughout 1400 redox cycles, in a bubbling fluidized bed reactor operated at 845 °C with space velocities varying between 2000 and 3250 hr<sup>-1</sup>. The pressure drop across the fluidized bed was also quite stable, indicating proper fluidization without significant attrition and particle entrainment<sup>129</sup>.

The demonstrated higher conversion, along with *in-situ* H<sub>2</sub> oxidation, leads to a lower energy requirement and potential for near an order of magnitude CO<sub>2</sub> emission reduction (**Figure 7b**).

While **Type 1** redox catalysts were most frequently used in the context of ethane thermal cracking, they can also be applied for oxidative cracking of naphtha. As shown in **Figures 8a and b**, the promotion of Na<sub>2</sub>WO<sub>4</sub> on BaFe<sub>6</sub>Al<sub>6</sub>O<sub>19</sub>, CaMnO<sub>3</sub>, or La<sub>0.8</sub>Sr<sub>0.2</sub>FeO<sub>3</sub> decreases the CO<sub>x</sub> selectivity and increases the olefin yields from the cracking of naphtha model compounds such as n-hexane and cyclohexane<sup>158-160</sup>.

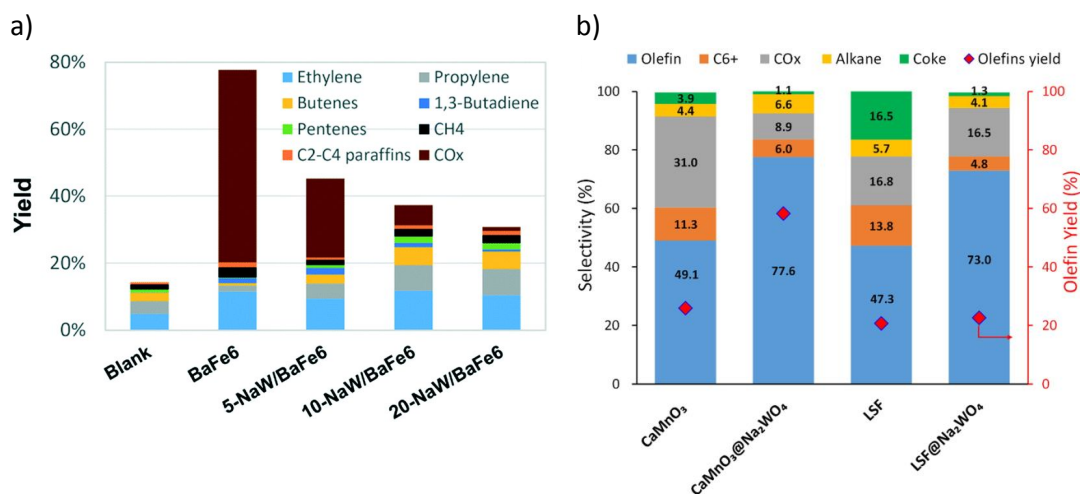


**Figure 8.** a) Products yields of BaFe<sub>6</sub>Al<sub>6</sub>O<sub>19</sub> after promotion with different amounts of Na<sub>2</sub>WO<sub>4</sub> in n-hexane cracking. Reaction condition: T = 700 °C; GHSV = 9000 h<sup>-1</sup> cyclohexane concentration ≈ 13 mol. %<sup>160b</sup>) Selectivity profile of cyclohexane cracking with Na<sub>2</sub>WO<sub>4</sub>@CaMnO<sub>3</sub> T = 750 °C; GHSV = 5400 h<sup>-1</sup>; cyclohexane concentration ≈ 7 mol. %<sup>158</sup>

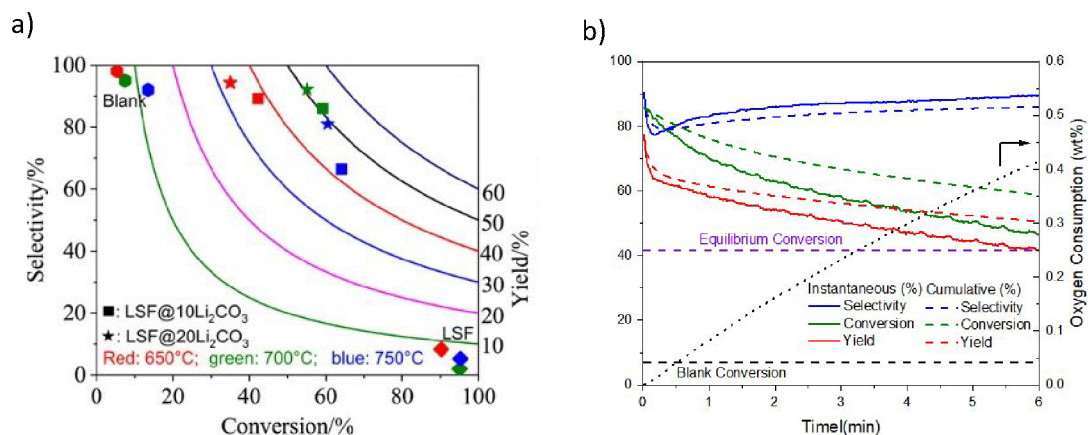
A similar strategy has also been recently adopted by a few other researchers in the context of CL-ODH and methane oxydehydroaromatizations<sup>96, 97, 118, 166</sup>. In all cases, higher H<sub>2</sub> combustion selectivity were observed after promoting the oxide surface with the “inert” molten salt. This further demonstrates the feasibility of the **Type 1** catalyst architecture. In fact, the selective hydrogen combustion function of **Type 1** redox catalyst would work well when combined with other DH or cracking catalysts. This will be further detailed in Section 2.3.

To sum up, the design of **Type 1** redox catalyst mainly aims to increase the selectivity towards hydrogen combustion, reducing the unwanted deep oxidation products such as CO<sub>x</sub>. We apply an “inert” layer of molten salt, which is largely inactive towards C-H bond activation, while still being able to selectively oxidize hydrogen using the active lattice oxygen from the transition metal oxides. The term inert mainly refers to the inhibition of C-H bond activation since the molten salt promoters do actively participate in oxygen and electron transport as well as the hydrogen combustion reaction.

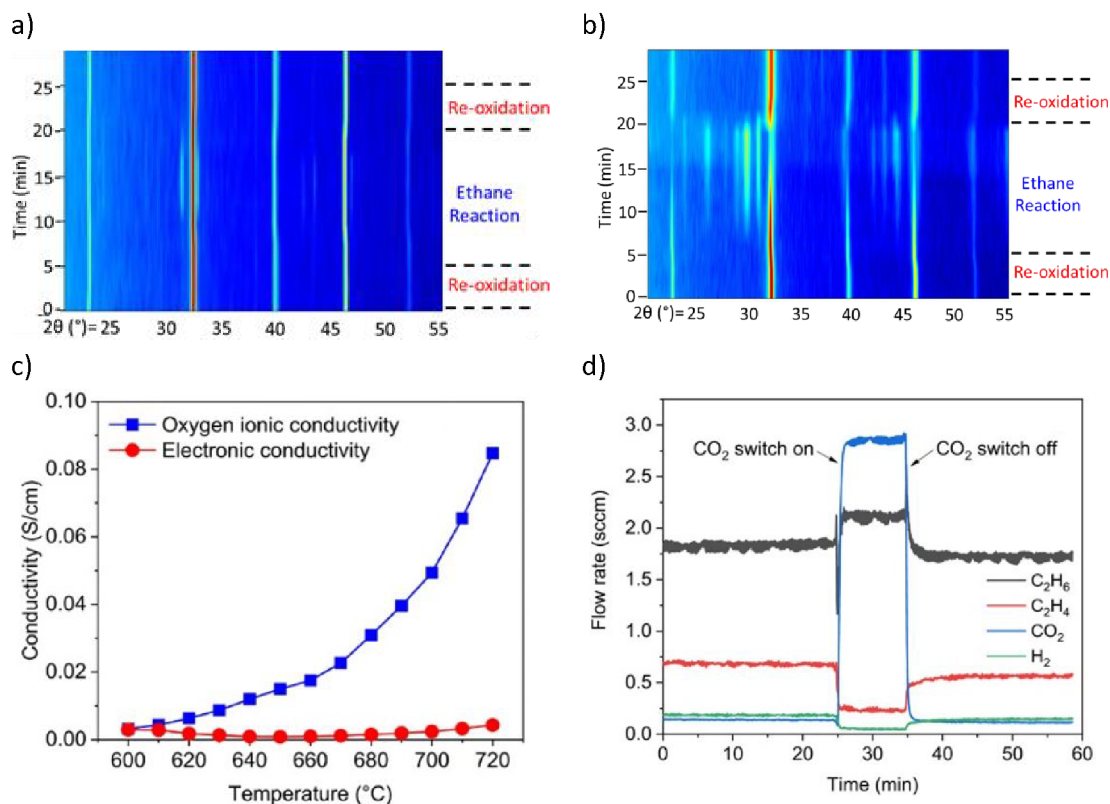
### 2.1.2. Type 2: Active molten salt modification

Contrasting the “inert” nature of the **Type 1** molten salt towards C-H bond activation, **Type 2** redox catalysts utilize an “active” molten salt promoter to accelerate the ODH reactions. This is facilitated by the active species such as peroxides and halogen atoms generated from the interaction with the mixed oxide core. Our recent studies indicate that many mixed oxides, e.g. La<sub>0.8</sub>Sr<sub>0.2</sub>FeO<sub>3-δ</sub> (LSF), when promoted by molten carbonate or halide salts, are quite effective

for CL-ODH of  $C_2$ - $C_4$  alkanes.<sup>167, 168</sup> Shown in **Figure 9a**, LSF@ $Li_2CO_3$  achieved >55% conversion and ~90%  $C_2H_4$  selectivity for CL-ODH of ethane at ~750 °C.<sup>167</sup> The time-dependent gaseous product profile within the ODH half cycle (**Figure 9b**) also demonstrated significantly higher ethane conversion than thermal cracking (denoted as blank). The molten  $Li_2CO_3$  shell also significantly increased the ethylene selectivity for the LSF core. Compared to the minimal activity in thermal cracking, the significant increase in conversion with the **Type 2** redox catalysts indicates that the molten salt layer catalyzes the ODH reactions besides its SHC function.



**Figure 9.** a) Ethylene selectivity and conversion profiles for LSF@10 wt. % (or 20 wt. %)  $Li_2CO_3$  via CL-ODH of ethane (our work) compared with literature results with various catalysts<sup>167</sup>; b) Ethane conversion profile vs. time-on-stream for: LSF@ $Li_2CO_3$ , thermal cracking (denoted as blank) and equilibrium conversion at 700 °C and 480 hr<sup>-1</sup>.



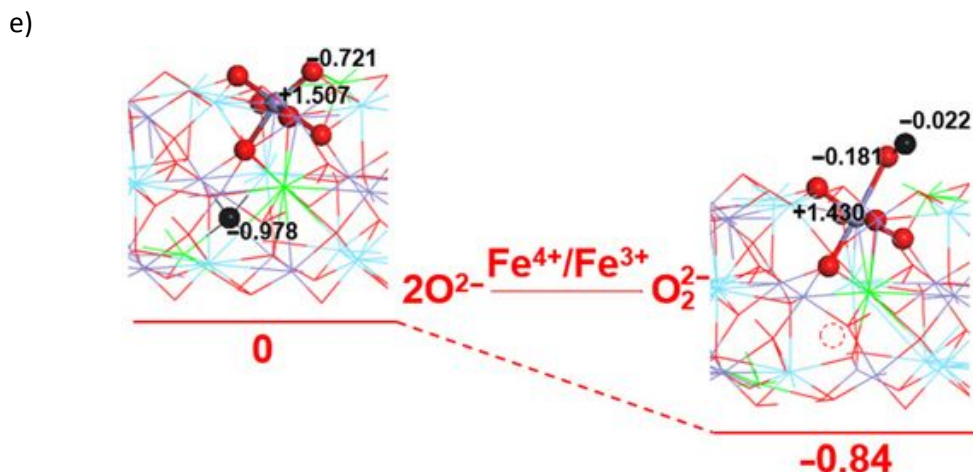


**Figure 10.** a) *in-situ* XRD of LSF@10 wt.%  $\text{Li}_2\text{CO}_3$  under CL-ODH cycles at 700 °C, the LSF phase remained stable, with a small amount of  $(\text{La}/\text{Sr})_2\text{FeO}_4$  formed during the ODH step; b) *in-situ* XRD of unpromoted LSF under CL-ODH cycles at 700 °C. Decomposition of the LSF phase to  $\text{La}_2\text{O}_3$ ,  $(\text{La}/\text{Sr})_2\text{FeO}_4$ , and Fe occurred during the ODH step; c) Electrochemical impedance spectroscopy (EIS) of  $\text{Li}_2\text{CO}_3$ ; d) Ethane and  $\text{O}_2$  co-feed experiment on pure  $\text{Li}_2\text{CO}_3$  with and without  $\text{CO}_2$  co-feed at 730°C, 4000  $\text{hr}^{-1}$ ; e) DFT calculation of peroxide formation with  $\text{Fe}^{4+}$  to  $\text{Fe}^{3+}$  transition <sup>167</sup>

*In-situ* XRD was performed to study LSF@10 wt. %  $\text{Li}_2\text{CO}_3$  (**Figure 10a**) and LSF (**Figure 10b**)<sup>167</sup>. The peak analysis indicates that the perovskite (LSF) phase largely remained stable in LSF@10 wt. %  $\text{Li}_2\text{CO}_3$  during the ODH step. In contrast, a significant portion of unpromoted LSF decomposed to  $\text{La}_2\text{O}_3$ ,  $(\text{La}/\text{Sr})_2\text{FeO}_4$  and Fe phases. TGA studies showed that the oxygen capacity of LSF@10 wt. %  $\text{Li}_2\text{CO}_3$  was significantly lower than pure LSF (0.5 wt. % vs. 12 wt. %). These observations indicate that  $\text{Li}_2\text{CO}_3$  inhibits the oxygen release from LSF and limits the reduction of Fe cation in the perovskite structure. Coupled with Mössbauer spectroscopy results, it was determined that for LSF@10 wt. %  $\text{Li}_2\text{CO}_3$ ,  $\text{Fe}^{4+}$  in LSF was reduced to  $\text{Fe}^{3+}$ , whereas in unpromoted LSF, a notable fraction of  $\text{Fe}^{4+}/\text{Fe}^{3+}$  were deeply reduced to form metallic Fe. The role of  $\text{Li}_2\text{CO}_3$  was further characterized by electrochemical impedance spectroscopy (EIS, **Figure 10c**). The results indicate that, at near melting point,  $\text{Li}_2\text{CO}_3$  has increased oxygen ion conductivity but the electronic conductivity stayed near zero. This suggests that  $\text{Li}_2\text{CO}_3$  could transport ionic oxygen species, but not electron. Therefore, such oxygen species must be in the oxidized form. Among all possible species, peroxide ion ( $\text{O}_2^{2-}$ ) is the most likely after excluding other potential species (molecular  $\text{O}_2$ ,  $\text{O}^{2-}$ ,  $\text{O}_2^-$ , and  $\text{C}_2\text{O}_4^{2-}$ ) based on  $\text{O}_2$ -TPD,  $^{13}\text{C}$ -NMR, and literature study<sup>169</sup>. This was also supported by the ethane and  $\text{O}_2$  co-feed experiment with and without co-feeding  $\text{CO}_2$  (**Figure 10d**). It was shown that the co-feed of  $\text{CO}_2$  would decrease the activity for ethylene formation, indicating that the peroxide species is likely suppressed by  $\text{CO}_2$  ( $2\text{O}_2^{2-} + 2\text{CO}_2 \rightarrow 2\text{CO}_3^{2-} + \text{O}_2$ ). Density functional theory (DFT) calculation also indicates that the formation of the peroxide from the  $\text{Fe}^{4+}$  to  $\text{Fe}^{3+}$  is thermodynamically favorable (**Figure 10e**). Based on these findings, the following reaction steps were proposed for the ODH reaction: (1) peroxide formation at the LSF/ $\text{Li}_2\text{CO}_3$  interface through  $\text{Fe}^{4+} \rightarrow \text{Fe}^{3+}$  transition; (2) dissolution and transport of the  $\text{O}_2^{2-}$  by  $\text{Li}_2\text{CO}_3$ ; (3) H abstraction from  $\text{C}_2\text{H}_6$  facilitated by  $\text{O}_2^{2-}$  at the molten-salt/gas interface. The subsequent reactions are likely to proceed through a surface initiated homogenous reaction pathway by releasing ethyl radicals into the gas phase.

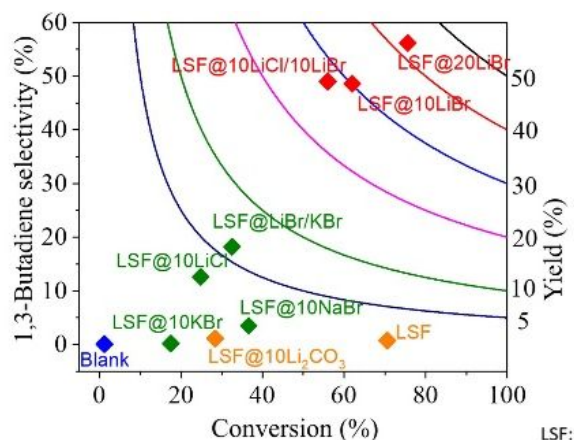


**Figure 11.** 1,3-butadiene selectivity and conversion profiles for LSF@10 wt. % LiBr via CL-ODH of n-butane (our work) compared with literature results with various catalysts at GHSV=4500 hr<sup>-1</sup> and 500 °C<sup>168</sup>;

As one would expect, for different reactions and conditions, the required active species may change. For example, butane ODH to 1,3 butadiene conversion needs to be carried out at temperatures far below Li<sub>2</sub>CO<sub>3</sub>'s melting point (~710 °C). As such, LSF@10 wt. % Li<sub>2</sub>CO<sub>3</sub> would not be effective. As can be seen from **Figure 11**, LSF@10 wt. % Li<sub>2</sub>CO<sub>3</sub> does not have a high selectivity towards 1,3-butadiene.<sup>168</sup> For this reaction, LSF@AX (A=alkali, X=halogen) redox catalysts showed significant butadiene yields whereas the blank experiment indicated minimal thermal cracking<sup>155</sup>. The unmodified LSF exhibited 71% butane conversion, but with ~93% selectivity towards CO<sub>x</sub> products. In contrast, LSF@20 wt. % LiBr showed 56.2% 1,3-butadiene selectivity with 75.6% n-butane conversion.<sup>168</sup>

Compared to LiBr, other molten and active halogenated salt promoters such as NaBr, KBr and/or LiCl were less effective. This indicates that Br possibly act in conjunction with Li to facilitate selective dehydrogenation of butane. The role and interaction of Li and Br species were probed by *ab initio* molecular dynamics (AIMD) shown in **Figure 12a**, the LiBr is likely oxidized by Li<sub>2</sub>O<sub>2</sub> to form atomic Br, which then diffuse to the surface and facilitate H abstraction from butane at the gas/molten salt interface. DFT calculation shown in **Figure 12b** indicates that the Br assisted C-H activation have energy barriers of 91.6 kJ/mol (butane to butyl radical) and 34.7 kJ/mol (1-butene to butenyl radical), a significant decrease compared to the C-H bond dissociation energy (~400 kJ/mol). In addition, the desorption energies of the radicals are both ~30 kJ/mol, it is therefore more likely that the radicals would be converted to the dehydrogenated counterpart on the surface of the molten salt layer. Additional gas-phase Reaction Mechanism Generator (RMG) and Chemkin-Pro results indicate the 2-butene, instead of 1,3-butadiene, would be the primary product via gas phase radical reactions in the presence of butyl radical. The absence of 2-butene rejects the surface initiated radical reaction pathway. As such, the as-formed atomic Br would be primarily responsible for all the dehydrogenation steps. Based on these findings, the following reaction steps were proposed: (1) the as-formed peroxide on LSF oxidizes Li<sub>2</sub>O to Li<sub>2</sub>O<sub>2</sub>; (2) Li<sub>2</sub>O<sub>2</sub> oxidizes LiBr to atomic Br; (3) Atomic Br then abstracts H from C-H bond from n-butane and 1-butene, sequentially forming 1,3-butadiene and HBr; (4) HBr then react with Li<sub>2</sub>O to form LiBr to complete the reaction cycle.

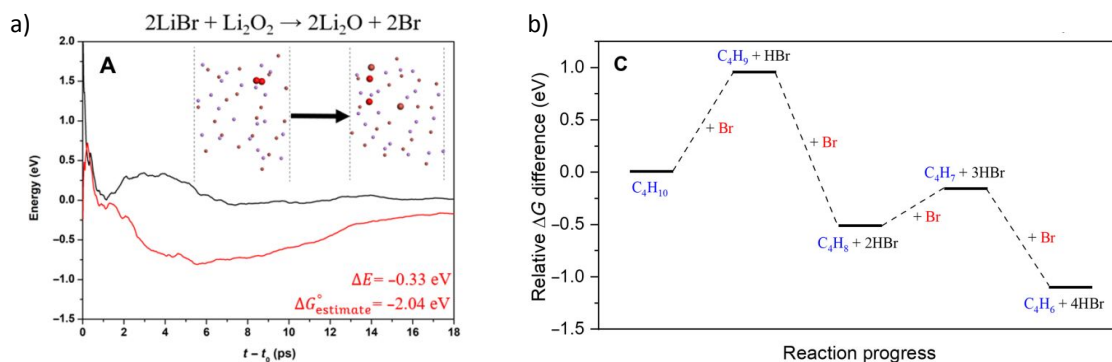


**Figure 12.** a) AIMD calculation of reaction pathway of  $2\text{LiBr} + \text{Li}_2\text{O}_2 \rightarrow 2\text{Li}_2\text{O} + 2\text{Br}$ ; b) AIMD calculation of reaction pathway of n-butane reacting with atomic Br-containing molten LiBr<sup>168</sup>

**Table 3.** Proposed reaction pathway in the solid/gas and gas/liquid interfaces

| $\text{C}_2\text{H}_6$ ODH with LSF@ $\text{Li}_2\text{CO}_3$  | $\text{C}_4\text{H}_{10}$ ODH with LSF@LiBr   |
|--|---|
| At the LSF/molten $\text{Li}_2\text{CO}_3$ interface:  | At the LSF-molten LiBr interface:   |
| $2\text{Fe}^{4+} + 2\text{O}^{2-} \rightarrow 2\text{Fe}^{3+} + \text{O}_2^{2-}$                               | $\text{O}_2^{2-} + 2\text{Li}_2\text{O} \rightarrow \text{O}^{2-} + \text{Li}_2\text{O}_2$  |
| At the gas-molten $\text{Li}_2\text{CO}_3$ interface:  | $\text{Li}_2\text{O}_2 + 2\text{LiBr} \rightarrow 2\text{Li}_2\text{O} + 2\text{Br}$  |
| Overall reaction:  | At gas-molten LiBr interface:   |
| $\text{C}_2\text{H}_6 + \text{O}_2^{2-} \rightarrow \text{C}_2\text{H}_4 + \text{O}^{2-} + \text{H}_2\text{O}$ | Lumped Rxns $\begin{cases} \text{C}_4\text{H}_{10} + 2\text{Br} \rightarrow \text{C}_4\text{H}_8 + 2\text{HBr} \\ \text{C}_4\text{H}_8 + 2\text{Br} \rightarrow \text{C}_4\text{H}_6 + 2\text{HBr} \end{cases}$ |
|  | $\text{Li}_2\text{O} + 2\text{HBr} \rightarrow 2\text{LiBr} + \text{H}_2\text{O}$   |

Generally speaking, a **Type 2** redox catalyst functions through: (1) inhibiting  $\text{CO}_2$  formation by covering the mixed oxide with the promoter, this aspect is similar to **Type 1** redox catalysts<sup>167, 168</sup>; (2) selectively catalyzing ODH reactions through the formation of active species from molten salt and oxide core interactions. It is also worth noting that different promoters in **Type 2** redox catalysts can lead to different reaction pathways and mechanisms (**Table 3**). Selection of the oxide substrate is also important in terms compatibility with the promoter and ability to form desirable active oxygen species such as peroxide ions.

## 2.2 Type 3: Mixed oxide @ catalytic phase redox catalyst for hydrocarbon conversion

**Type 3** redox catalysts are based on a design concept like **Type 2** but differs in that a solid catalytic phase is used and a radical formation step is not likely to be involved. For instance, a well-studied K-Fe-O catalyst is highly active towards ethylbenzene DH to styrene<sup>170, 171</sup>. By combining the K-Fe-O's catalytic function with transitional metals oxides' SHC capability, equilibrium limitation can be circumvented, intensifying the overall process.

A notable example is the multi-functional  $(\text{Ca}/\text{Mn})_{1-x}\text{O}@\text{KFeO}_2$  redox catalyst developed from our group, which showed high activity towards ethylbenzene CL-ODH<sup>161</sup>. As shown in **Figure 13a**, up to 91% single-pass styrene yield can be achieved. This represents a 72% yield increase, on a relative basis, compared to commercial dehydrogenation. As can be seen in **Figure 13a**,

there is an unselective region at the beginning of the ODH reaction step, during which the ST selectivity was  $\sim 54\%$ . The selectivity of ST would increase to  $\sim 95\%$  as more ethylbenzene (EB) is injected. This unselective region can be avoided by limiting the air injection during the regeneration step, as shown in **Figure 13b** to maintain a high selectivity ( $\sim 94.2\%$ ). Higher EB partial pressures closer to industrial conditions has also been tested at a lab scale (**Figure 13c**), and the styrene yield surpassed the equilibrium limitation. In addition, the stability of this redox catalyst was tested for 100 cycles (**Figure 13d**), albeit at a relatively low EB partial pressure.

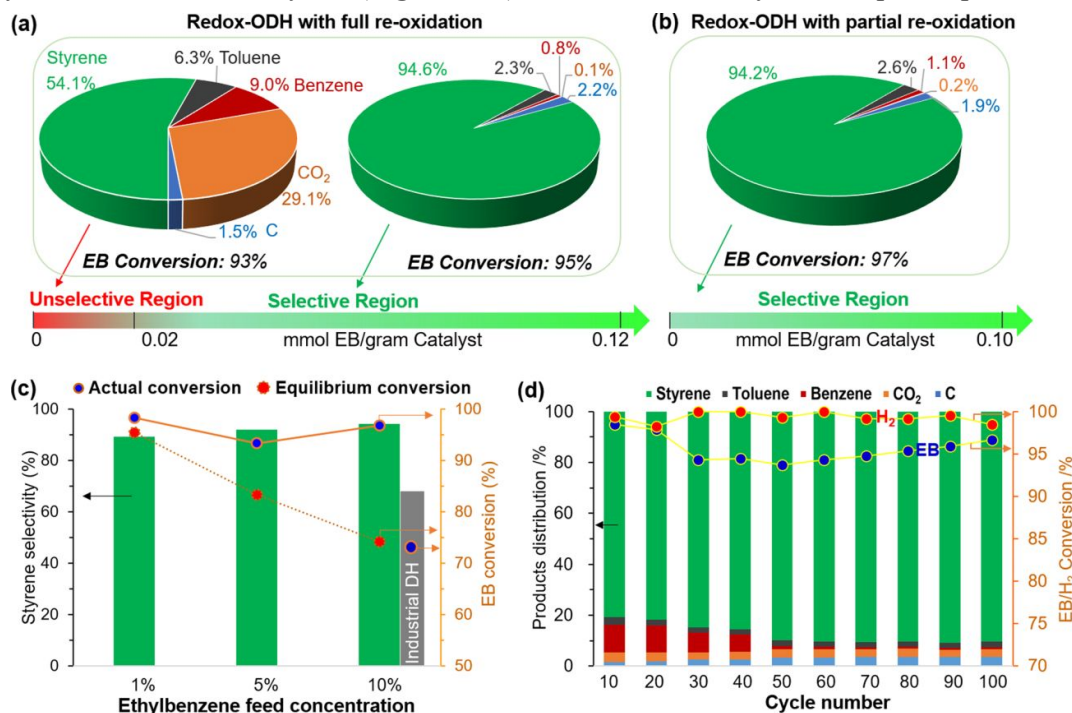


**Figure 13** Performance of redox-ODH of ethylbenzene with a) fully reoxidized and b) partially reoxidized redox catalyst (EB partial pressure =  $\sim 0.01$  atm, temperature =  $600$  °C). c) Redox-ODH performance comparing to DH equilibrium conversions in the range of  $0.01$ – $0.1$  atm ethylbenzene feed partial pressure (balance Ar) using partially reoxidized redox catalyst. d) Long-term cycle and product distributions in redox-ODH using fully reoxidized redox catalyst.<sup>161</sup>

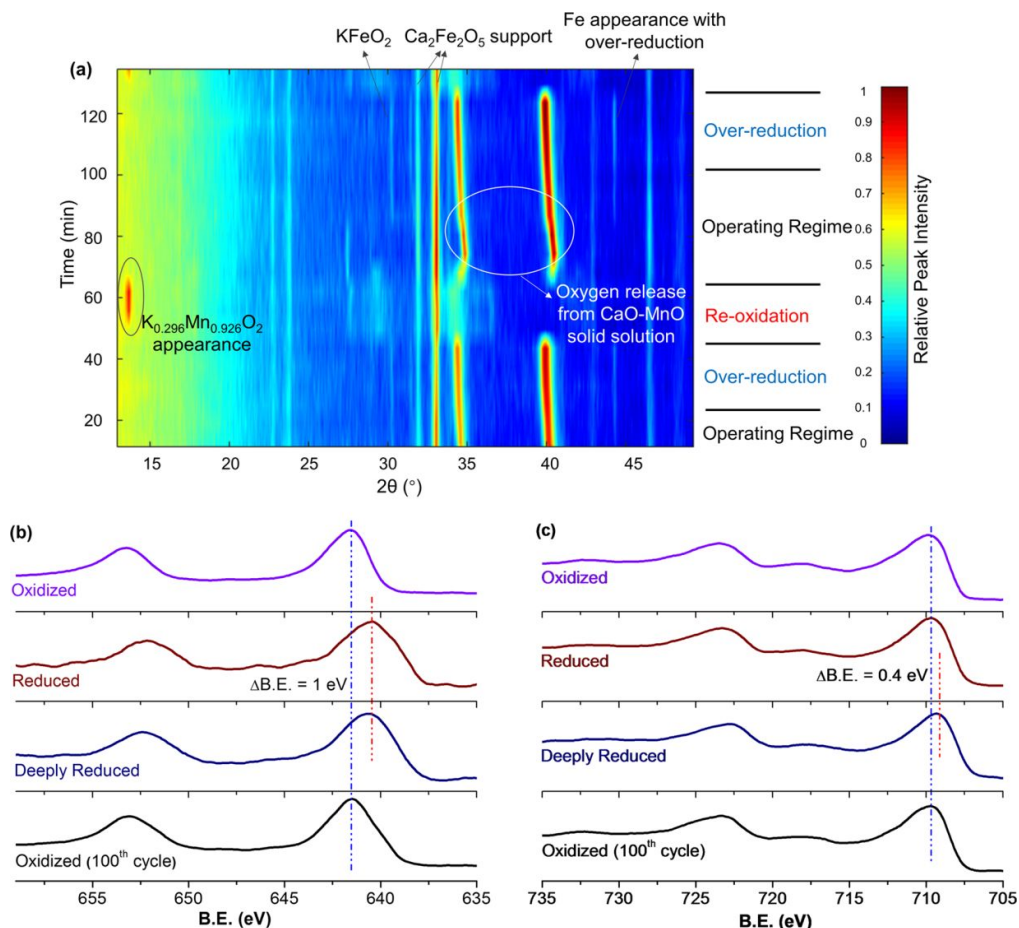


**Figure 14.** a) In situ XRD under cyclic ethylbenzene ODH and air reoxidation steps at 600 °C; b) XPS of Mn 2p and c) XPS of Fe 2p for redox catalysts at different reaction stages.<sup>161</sup>

**Figures 13a and b** signify that there were dynamic changes in the redox catalyst. *in-situ* XRD (**Figure 14a**) and *ex-situ* XPS (**Figure 14b**) were used to characterize the changes in the shell and the core at different stages of the redox ODH reactions<sup>161</sup>. *In-situ* XRD indicated that the unselective region shown in **Figure 13a** was resulted from the solid-state reactions between the core and shell phases, forming a nonselective  $K_{0.296}Mn_{0.926}O_2$  phase while decreasing the surface concentration of potassium. As the injection of EB continues, this nonselective phase disappeared and the catalytic layer  $KFeO_2$  appeared throughout the rest of the EB injection step. Meanwhile, there was a continuous lattice oxygen release from the  $CaO-Mn^{2+/3+}O$  solid solution, which was responsible for selective hydrogen combustion. From **Figures 14b and c**, the Mn 2p peaks shifted to lower binder energy level when in contact with EB (in both reduced and deeply reduced region), while the Fe 2p peaks only shifted after *prolonged* contact with the EB (deeply reduced region). Both results suggest that  $Fe^{3+}$  oxidation state, which is key to high DH activity, is reserved by sacrificing  $Mn^{3+/4+}$  in the operating regime.

The reaction mechanism was further studied by isotope experiments in our group. Similar to conventional catalytic DH, during the dehydrogenation reaction, ethylbenzene on the CLCa catalyst undergoes a two-step H abstraction on the  $KFeO_2$  surface<sup>170-172</sup>. The KIE value (**Figure 15a**) measured in the isotope experiment confirmed that H abstraction was the rate limiting

step. This was further supported by the DFT results (**Figure 15b-1**), where the  $\alpha$ -H abstraction step was shown to be rate limiting. DFT results also indicated that the presence of water would facilitate the proton transfer in the water formation step on the  $\text{KFeO}_2$  surface, leading to more than 4-fold decrease in activation energy (**Figure 15b-2**). This was verified by dehydrogenation experiments on  $\text{KFeO}_2$  both with and without cofeeding steam.

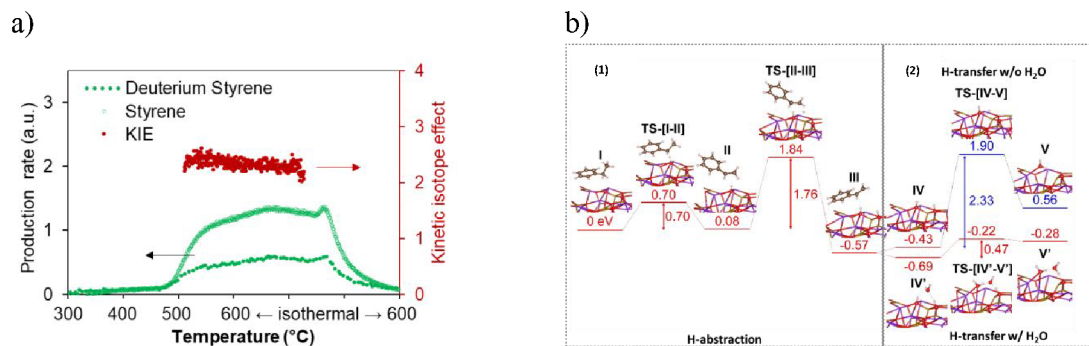


**Figure 15.** a) Kinetic isotope effect study with both temperature-programmed reduction and isothermal reduction of the  $(\text{Ca/Mn})_{1-x}\text{O}@K\text{FeO}_2$  using  $\text{C}_8\text{H}_{10}$  and  $\text{C}_8\text{D}_{10}$ <sup>161</sup>; b) Computed energy potential profiles of (1)  $\alpha$  and  $\beta$  H abstraction and (2) proton transfer and water formation with or without water assistance<sup>161</sup>

Similar to **Type 2** redox catalysts, design of **Type 3** needs to consider the compatibility of the core and shell materials. The dynamic changes observed during the redox reactions signifies the potential complexity of CLCa when compared to conventional heterogeneous catalysis systems.<sup>161</sup>

### 2.3 Synergistic effects between heterogeneous and redox catalysts

As briefly mentioned in **Section 2.1**, the abovementioned redox catalyst design, particularly **Type 1**, has the potential to function in concert with conventional heterogeneous catalysts. We recently demonstrated this approach towards catalytic cracking of cyclohexane by integrating cation exchanged ZSM-5 with a **Type 1** redox catalyst, i.e.  $\text{Na}_2\text{WO}_4$  promoted perovskite oxide<sup>157</sup>. The primary function of the redox catalyst was to selectively oxidize hydrogen and to enhance the naphtha conversion. It is interesting to note that a significant increase in ethylene ( $\text{C}_2^=$ ) and propylene ( $\text{C}_3^=$ ) selectivity and  $\text{C}_3^=/\text{C}_2^=$  ratio was observed by mixing the ZSM-5 based catalyst with the Type 1 redox catalyst (**Figures 16a and b**). The presence of the  $\text{Na}_2\text{WO}_4 @$  perovskite catalyst did not deactivate the zeolite catalyst. Rather, it changed the acidic properties of the zeolite by creating additional strong Brønsted acid sites, which is likely to be responsible for the enhanced olefin selectivity and yield. A similar concept was also shown to be effective for *n*-hexane conversion: Ba-exchanged ZSM5 mixed with  $\text{CaMnO}_3@Na_2\text{WO}_4$  could exhibit up to 67% single-pass olefin yield from *n*-hexane with tunable propylene to ethylene ratio, with <5%  $\text{CO}_2$  yield<sup>173</sup>. We note that in both cases, the nature of the interactions between ZSM-5 and the redox catalyst particles, as well as the fundamental reasons for the change in product selectivity have yet to be understood<sup>157</sup>. This represents an interesting area for in-depth studies. Synergistic utilization of heterogeneous catalysts with redox-active oxides can also significantly broaden the applicability for CLCa.

When integrating CLCa with a heterogeneous catalyst, an important aspect to consider is whether the heterogeneous catalyst would function well under significant oxygen partial pressure swings. In addition, steam generated from hydrogen combustion by the CLCa redox

catalyst can have a negative impact on the active sites of the catalyst and can lead to side reactions (e.g. steam reforming). For example,  $\text{MoC}_x$ , active for dehydroaromatization (DHA) of methane<sup>174-181</sup>, can react with steam produced from SHC to form  $\text{MoO}_x$ , which would deactivate the catalyst. Therefore, care must be taken in selecting robust and compatible hybrid catalyst systems involving both chemical looping and heterogeneous catalysis.

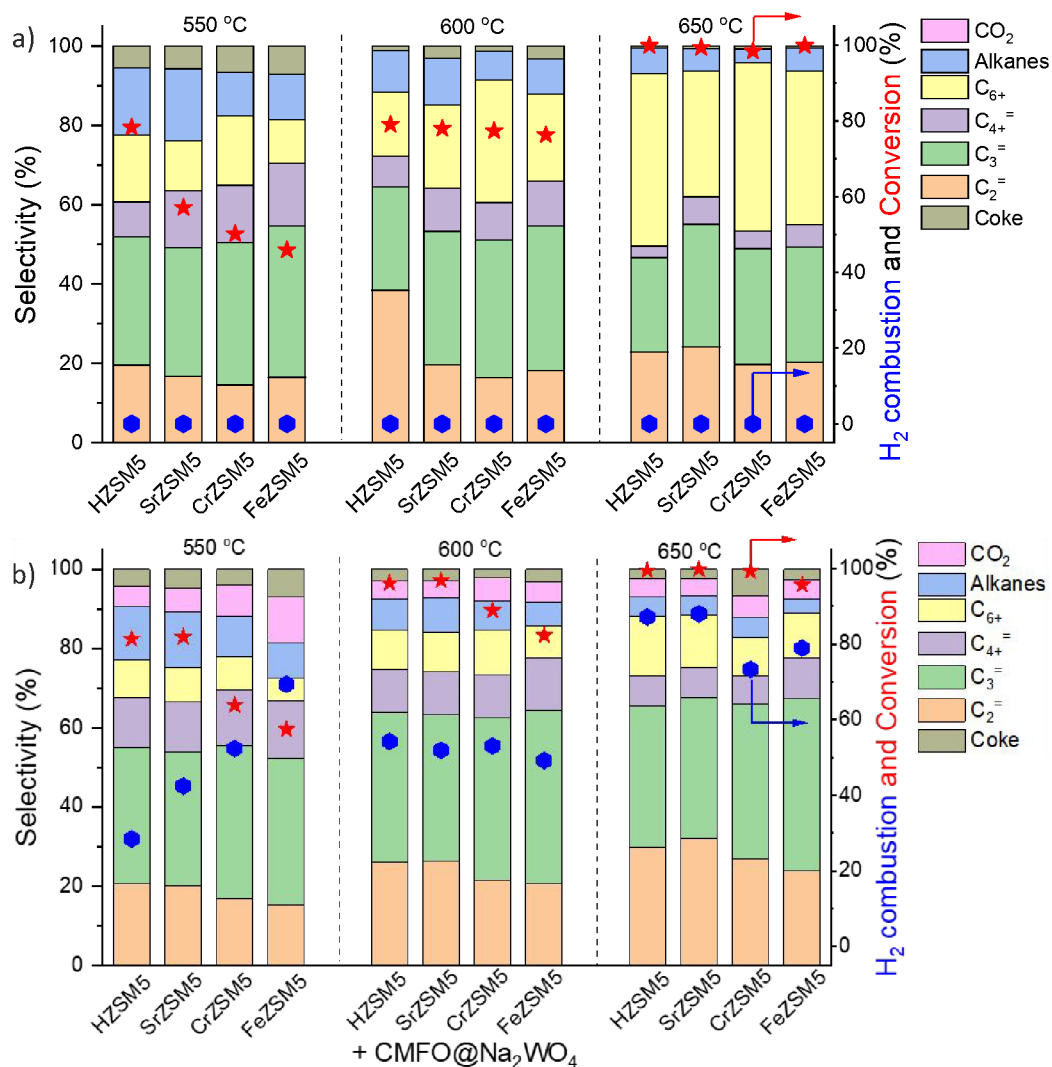


**Figure 16.** Cyclohexane conversion and product distributions over a) HZSM5 and different metal cation (Sr, Ca, Cr or Fe) exchanged ZSM-5; b) composite composed of ZSM-5s and  $\text{CaMn}_{0.75}\text{Fe}_{0.25}\text{O}_{3-\delta}@\text{Na}_2\text{WO}_4$  redox catalyst<sup>157</sup>;

## 2.4 Computational assisted oxide selection

Although the previous section focused on surface promoters for the redox-active oxides, the selection of the oxide also represents a crucial and enabling step to CL-ODH. In fact, a sizable amount of chemical looping research focused on discoveries and the selections of oxide-based oxygen carriers. To date, over 2,000 research articles have covered different aspects of oxygen carrier compositions, performance, and underlying mechanism. Despite the extensive research and development efforts, a rationalized strategy for the effective design and selection of oxygen

carriers is still lacking. In fact, the high complexity of redox reactions, which extends beyond the interactions of gaseous molecules with poorly defined oxide surfaces, makes it near impossible for *ab-initio* design of redox-oxides. On the other hand, the emergence of oxygen carriers composed of redox-active mixed oxides, e.g. perovskite oxides, has greatly expanded the design space for chemical looping material selection, making oxygen carrier optimization an even more daunting task.

We note that while it is impractical to expect an *ab-initio* oxygen carrier selection model to comprehensively consider all aspects of oxygen carrier design, some relatively simple selection criteria can nevertheless be adopted, particularly when capitalizing on modern computational and data science tools, to greatly reduce the experimental efforts in oxygen carrier development. Take CLCa of light alkanes as an example, the light olefin yields tie directly with the equilibrium oxygen partial pressure ( $P_{O_2,eq}$ ) or equivalently oxygen chemical potential ( $\mu_{O_2,eq}$ ) of the redox oxide from a thermodynamic standpoint (**Figure 17a**). In fact, the thermodynamic selection rule of the oxides in CLCa of alkane ODH largely overlaps with that of chemical looping combustion and chemical looping air separation (CLAS). This is not at all surprising given that a primary function of the oxygen carrier in CLCa is *in-situ* air separation, besides acting as a heterogeneous catalyst. Given that the thermodynamic requirement represents a prerequisite for oxygen carrier selection, we recently used such a criterion to select oxides with a general formulation of  $Sr_xA_{1-x}Fe_yB_{1-y}O_{3-\delta}$  ( $A = Ca, K, Y, Ba, La, Sm$ ;  $B = Ti, Ni, Mn, Mg, Cu, Co$ ) for applications such as CLAS and chemical looping dry reforming of methane. **Figure 17b** illustrates the generalized simulation and experimental validation strategies as well as representative results.<sup>182</sup> Despite adopting simplified assumptions to facilitate density functional theory (DFT) based high throughput computations, the simulation results were shown to be quite effective in predicting various perovskite oxides with interesting properties, that could be adopted in the both CLAS or CLCa<sup>182</sup>. These redox active oxides materials have excellent potential to be adopted for CLCa. We also note that the proposed model is not without limitations. For instance, the model was based exclusively on thermodynamic criteria without considering kinetic effects. To ensure manageable computational intensity, we assumed random distribution of the dopants and did not consider potential defect clustering. The U parameters selected to correct the strong on-site coulomb interaction of the d-electrons may need to be further tuned for the perovskite oxides. Potential formation of alternative phases and structures besides the base  $SrFeO_3$  structure were not considered. These represents potential areas of improvements for future modelling efforts. To date, only a few other groups have also use high-throughput method for materials screening<sup>183, 184</sup>. Fan et al. screened over 1500  $M_1$ - $M_2$ -O/N pairs and 170  $M_1$ - $M_2$ - $N_{rich}/N_{poor}$  pairs to identify optimized bicationic materials for CL-ammonia synthesis from different route<sup>183</sup>. In the context of CLC of methane, Singstock et al. screened over 1300 redox pairs (i.e.  $ABO_x/AO_y+B$ ,  $A(SO_4)_x/AS_x$ ) and predicted 152 pair to demonstrate >99% methane conversion with limited byproducts<sup>184</sup>.

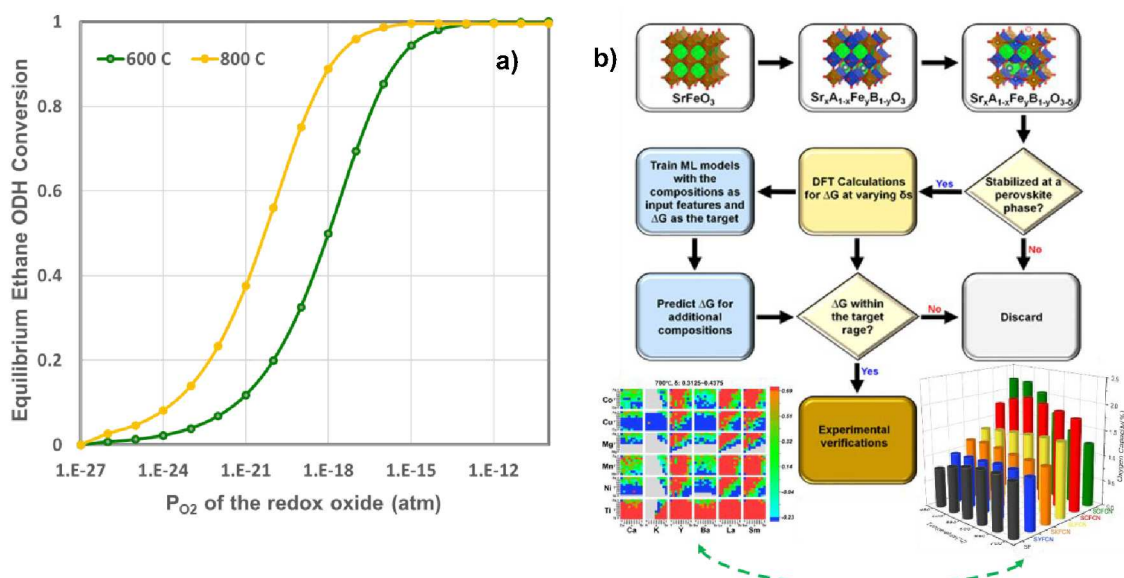


**Figure 17.** a) Relationship between the equilibrium ethane conversion in CL-ODH and the equilibrium  $P_{O_2}$  of the redox oxide at 600 and 800 °C (only the ODH reaction is considered in this calculation without considering the dehydrogenation reaction); b) a general strategy for computationally guided oxide selection and the key results related to CLAS material selection published by Wang et. al.<sup>182</sup>;

### 3 Summary and outlook

The pressing need for decarbonizing the modern society calls for transformative technologies to intensify state-of-the-art manufacturing processes. The chemical looping strategy, with an inherent capability for chemical transformation combined with feedstock and/or product separations, offers unique opportunities to significantly simplify the chemical manufacturing processes, improve energy efficiency, and reduce  $CO_2$  emissions.

This review covered a generalized redox catalyst design strategy, involving a redox-active mixed metal oxide core and a surface promoter shell, for the CL-ODH of hydrocarbons to olefins. An interesting aspect of this design strategy is the ability to independently tune the properties of the oxide core and the promoter shell provided that the two materials are compatible under the operating conditions. For example, for ethane conversion with **Type 1** catalyst, we recently predicted that  $C_{2+}$  yield could achieve 78.2 – 86.7% based on the existing data from molten salt promoted  $Mg_6MnO_8$  and  $Cu/MnO_x$ . These analyses suggest that further increase in single-pass olefin yield is highly possible by optimizing the core and the shell compositions and ratios. For **Type 2** redox catalysts, the heat of reactions of ethane CL-ODH can be tuned to be mildly exothermic in both the ethane ODH and the re-oxidation steps, allowing more efficient heat management. On the other hand, the selection of the core would also affect the activity and selectivity of the redox catalysts. In the case of LSF,  $Fe^{4+}$  in the perovskite structure was proposed to be responsible for the formation of the peroxide in molten phase. As an example, further adjusting the La:Sr ratio could tune the propensity to form peroxide and therefore optimize the ODH performance. **Type 3** redox catalysts, and the

potential to integrate CLCa redox catalyst with a heterogeneous catalyst in tandem, also offer exciting opportunities.

From a practical standpoint, molten salt promoted oxides may not be easily fluidizable. However, it is possible to adjust the surface promoter compositions to ensure good fluidization properties and long-term stability<sup>129</sup>. Molten salt promoted redox catalysts have also been operated in packed bed reactors in our recent studies, showing satisfactory long-term stability up to 1,000 hours<sup>119, 120</sup>. Other issues to consider for future studies and practical applications include the potential vaporization of molten salts at high temperatures and reactor material selection to minimize potential corrosion. A recent long term study on Li<sub>2</sub>CO<sub>3</sub> promoted LSF showed signs of slight increase in CO<sub>x</sub> selectivity<sup>119</sup>. This may be attributed to the loss of Li<sub>2</sub>CO<sub>3</sub>. Therefore, replenishing of Li<sub>2</sub>CO<sub>3</sub> either *ex-situ* or during the reactor operation may be considered for future studies.

**Table 4.** Selected example of recent progress in chemical looping catalysis

| Target Product                    | Carrier   | Operating Condition  | Key Performance Result  | Ref            |
|-----------------------------------|---|--|---|----------------|
| Syngas/CO                         | Fe <sub>2</sub> O <sub>3</sub> @SBA-15  | 750-935 °C, 17.8-37.5 ml/h/mgFe <sub>2</sub> O <sub>3</sub>  | ~100% CO selectivity  | <sup>108</sup> |
|                                   | La <sub>0.5</sub> Ce <sub>0.5</sub> FeO <sub>3</sub>  | 850 °C, Flow rate: 80 ml/min<br>0.8 g catalyst<br>Reduction: 10 mol. % CH <sub>4</sub> /N <sub>2</sub><br>Oxidation: 10 mol. % CO <sub>2</sub> /N <sub>2</sub> | X <sub>methane</sub> : 82%<br>S <sub>Syngas</sub> : 93%                             | <sup>185</sup> |
|                                   | BaFe <sub>1-x</sub> Sn <sub>x</sub> O <sub>3-δ</sub>  | 900 °C, 0.1g catalyst<br>Reduction: 5% CH <sub>4</sub> /He (20 mL/min)<br>Oxidation: 5% O <sub>2</sub> /He (20 mL/min)   | >99% syngas selectivity<br>Y <sub>syngas</sub> = 19.2 mmol/g                        | <sup>114</sup> |
|                                   | MgO supported<br>Ca <sub>2</sub> Fe <sub>2</sub> O <sub>5</sub>   | 1000 °C, 2g catalyst 1500 hr <sup>-1</sup><br>Reduction: 10% CH <sub>4</sub> /He (25 mL/min)<br>Oxidation: 40% CO <sub>2</sub> /He (25 mL/min)                 | X <sub>methane</sub> >99%<br>S <sub>Syngas</sub> : 98.1%, H <sub>2</sub> /CO<br>~2  | <sup>117</sup> |
|                                   | Ni-doped<br>Fe <sub>2</sub> O <sub>3</sub> /Al <sub>2</sub> O <sub>3</sub>                                      | 900 °C, 2g catalyst 1500 hr <sup>-1</sup><br>Reduction: 20% CH <sub>4</sub> (75 mL/min)<br>Oxidation: 20% O <sub>2</sub> (75 mL/min)                           | X <sub>methane</sub> >95%<br>S <sub>Syngas</sub> : ~96%, H <sub>2</sub> /CO<br>~2.3 | <sup>186</sup> |
| Ethylene<br>(via CL-OCM)          | (Li,W)-Mg <sub>6</sub> MnO <sub>8</sub>   | 850 °C, 2400 h <sup>-1</sup><br>Reduction: Pure% CH <sub>4</sub> (200 mL/min)  | X <sub>methane</sub> : 50%<br>C <sub>2+</sub> Yield: 28.6%                          | <sup>106</sup> |
| Ethylene<br>(via CL-ODH)          | 0.2Ce/SrFeO <sub>3</sub>  | 700~750 °C 3000~6000 h <sup>-1</sup><br>Reduction: ~12.5 mol.% C <sub>2</sub> H <sub>6</sub>   | Ethylene Yield: 23.8%<br>X <sub>CO2</sub> 69.4%                                     | <sup>100</sup> |
|                                   | Sr <sub>0.8</sub> Ca <sub>0.2</sub> FeO <sub>3-δ</sub> @Na <sub>2</sub> CO <sub>3</sub> + MoVNbTeO <sub>x</sub> | 500 °C, 600 h <sup>-1</sup> GHSV<br>Reduction: 6 mol. % C <sub>2</sub> H <sub>6</sub> , balance N <sub>2</sub>   | S <sub>ethylene</sub> : 91%<br>X <sub>ethane</sub> : 42%                            | <sup>96</sup>  |
|                                   | Ce-incorporated<br>FeTiO <sub>x</sub>   | 600 °C,<br>Reduction: 20 vol. % C <sub>2</sub> H <sub>6</sub> /N <sub>2</sub> , 30ml/min<br>Oxidation 20 vol. % CO <sub>2</sub> /N <sub>2</sub> , 30 ml/min    | S <sub>ethylene</sub> : 84.1%<br>X <sub>ethane</sub> : 14%                          | <sup>187</sup> |
| Propylene<br>(via CL-ODH)         | Mo-V-O<br>(V/Mo=6) <sup>188</sup>   | 500 °C, 2500 h <sup>-1</sup> GHSV<br>Reduction: Pure% CH <sub>4</sub> (200 mL/min)   | X <sub>propane</sub> : 36%<br>S <sub>propylene</sub> : 89%                          | <sup>188</sup> |
| Ammonia                           | Li-Pd/Li <sub>2</sub> NH  | 300 °C and 1 bar<br>100% N <sub>2</sub> or H <sub>2</sub> at 30 ml/min   | r <sub>NH<sub>3</sub></sub> = 693 μmol <sub>NH<sub>3</sub></sub> g <sup>-1</sup> h  | <sup>189</sup> |
|                                   | Si modified γ-Al <sub>2</sub> O <sub>3</sub><br>ZrO <sub>2</sub> supported                                      | 1 bar<br>N-sorption: 1200 °C 100 ml/min N <sub>2</sub><br>NH <sub>3</sub> -desorption: 1200 °C 80 vol.% H <sub>2</sub> O 500 ml/min                            | X <sub>AIN</sub> =60.4%   | <sup>190</sup> |
|                                   | 20 wt. %TiN/MgO   | Nitridation: 1 atm, 808 nm laser at 30W/cm <sup>2</sup><br>(~550 °C)   | r <sub>NH<sub>3</sub></sub> = 1.67 μmol <sub>NH<sub>3</sub></sub> g <sup>-1</sup> h | <sup>191</sup> |
| NO<br>(NH <sub>3</sub> oxidation) | V <sub>2</sub> O <sub>5</sub>   | 300~650 °C<br>Reduction: 5 mol.% NH <sub>3</sub> /Ar, 30 ml/min<br>Oxidation: 30 mol.% O <sub>2</sub> /Ar, 30 ml/min   | NO selectivity: 99.8%<br>NH <sub>3</sub> conversion: 97%                            | <sup>192</sup> |

The application of chemical looping concept is not limited to olefin productions. **Table 4** summarizes recent publications related to CLCa. An extensively investigated topics is methane to syngas/H<sub>2</sub> conversion<sup>95, 109-117, 123, 125-127, 130, 136, 185, 193-208</sup>. A few other studies explored a phase transition sorbent concept where a single mixed oxide particle combines the function of a redox oxide (for oxygen separation), a carbonate sorbent (for CO<sub>2</sub> separation), and a catalyst (to catalyze chemical reactions)<sup>95, 123, 130, 197, 198, 209-211</sup>. For instance, a recent study adopted the chemical looping strategy to selectively oxidize ammonia with excellent NO selectivity for nitric acid production<sup>192</sup>. A few other studies explored the feasibility of using nitrides/imides/hydrides<sup>131-134, 189-191, 212-214</sup> as intermediates for ammonia synthesis and using alkali molten salt as the medium for combined CO<sub>2</sub> capture and utilization<sup>215</sup>. Engineering the chemical potential of redox oxides has also shown to be able to circumvent reaction equilibrium limitations in conventional processes while maintaining high selectivity, making it possible to achieve previously unattainable yields for water gas shift reactions<sup>126, 194</sup>. From the chemical looping standpoint, one can see that most of the processes summarized above harness the oxidizing potential (e.g. SHC) of the metal oxides at high temperatures during the half cycle for metal oxide reduction.

In most of the abovementioned processes, the reduced metal oxides are regenerated in an O<sub>2</sub>, CO<sub>2</sub>, or steam rich environment, allowing integrated air separation, CO<sub>2</sub>-splitting, or hydrogen production. It can be fully anticipated that well-designed metal oxides, after reduction, could be used for producing complex, value-added chemicals via hydrogenation and/or carbonylation during the regeneration half cycle. This offers the potential to produce two different value-added products in a two-step redox process or even multi-step chemical loops. Therefore, many new and highly exciting areas of fundamental research and practical applications can be anticipated through the unique combination of chemical looping with heterogeneous catalysis.

## 4 Acknowledgement

This work was supported by the U.S. National Science Foundation (Award No. CBET-2116724 and CBET-1923468), US Department of Energy (Award No. FE0031869, EE0008809, FE0031918), and the Kenan Institute for Engineering, Technology and Science at NC State University.

## 5 References

1. International Energy Agency, Chemicals, <https://www.iea.org/fuels-and-technologies/chemicals>, (accessed July 23rd, 2022).
2. I. E. Agency, Net Zero by 2050, <https://www.iea.org/reports/net-zero-by-2050>).
3. T. Ren, M. Patel and K. Blok, *Energy*, 2006, **31**, 425-451.
4. H. A. Maddah, *American Academic Scientific Research Journal for Engineering, Technology, and Sciences*, 2018, **45**, 49-63.
5. A. Agarwal, D. Sengupta and M. El-Halwagi, *ACS Sustainable Chemistry & Engineering*, 2018, **6**, 2407-2421.
6. H. Kim, B. Lee, D. Lim, C. Choe and H. Lim, *Green Chemistry*, 2021, **23**, 7635-7645.

7. R. C. Müller, A. Schiessl, R. Volk and F. Schultmann, *Journal of Cleaner Production*, 2021, **317**.
8. S. Yuanyuan, W. Di, Y. Junjie and Z. Liang, *Acta Petrolei Sinica(Petroleum Processing Section)*, 2020, **36**, 1361-1369.
9. A. C. Dimian and C. S. Bildea, *Industrial & Engineering Chemistry Research*, 2019, **58**, 4890-4905.
10. W. L. Luyben, *Industrial & Engineering Chemistry Research*, 2010, **50**, 1231-1246.
11. G. Rochelle, E. Chen, S. Freeman, D. Van Wagener, Q. Xu and A. Voice, *Chemical engineering journal*, 2011, **171**, 725-733.
12. E. Krzystowczyk, V. Haribal, J. Dou and F. Li, *ACS Sustainable Chemistry & Engineering*, 2021, **9**, 12185-12195.
13. J. Bao, Z. Li and N. Cai, *Industrial & Engineering Chemistry Research*, 2013, **52**, 6119-6128.
14. L. Xu, R. Edland, Z. Li, H. Leion, D. Zhao and N. Cai, *Energy & Fuels*, 2014, **28**, 7085-7092.
15. H. Gu, L. Shen, J. Xiao, S. Zhang and T. Song, *Energy & Fuels*, 2010, **25**, 446-455.
16. A. M. Kierzkowska and C. R. Müller, *ChemPlusChem*, 2013, **78**, 92-100.
17. Z. T. Yaqub, B. O. Oboirien, M. Hedberg and H. Leion, *Chemical Engineering & Technology*, 2021, **44**, 1075-1083.
18. D. Yilmaz, B. M. Steenari and H. Leion, *ACS Omega*, 2021, **6**, 16649-16660.
19. L. Liu, Z. Li, L. Wang, Z. Zhao, Y. Li and N. Cai, *Industrial & Engineering Chemistry Research*, 2019, **59**, 7238-7246.
20. J. Yan, H. Ge, S. Jiang, H. Gu, T. Song, Q. Guo and L. Shen, *Energy & Fuels*, 2019, **33**, 2153-2165.
21. Y. Li, H. Wang, W. Li, Z. Li and N. Cai, *Energy & Fuels*, 2018, **33**, 449-459.
22. T. Pröll and A. Lyngfelt, *Energy & Fuels*, 2022, **36**, 9502-9512.
23. D. Mei, A. Lyngfelt, H. Leion, C. Linderholm and T. Mattisson, *Energy & Fuels*, 2022, **36**, 9470-9484.
24. S. Bhavsar, M. Najera, A. More and G. Veser, in *Reactor and Process Design in Sustainable Energy Technology*, 2014, DOI: 10.1016/b978-0-444-59566-9.00007-7, pp. 233-280.
25. I. Gogolev, C. Linderholm, D. Gall, M. Schmitz, T. Mattisson, J. B. C. Pettersson and A. Lyngfelt, *International Journal of Greenhouse Gas Control*, 2019, **88**, 371-382.
26. H. Chen, M. Cheng, L. Liu, Y. Li, Z. Li and N. Cai, *International Journal of Greenhouse Gas Control*, 2020, **93**.
27. T. Song, E.-U. Hartge, S. Heinrich, L. Shen and J. Werther, *International Journal of Greenhouse Gas Control*, 2018, **70**, 22-31.
28. D. C. Ozcan, A. Macchi, D. Y. Lu, A. M. Kierzkowska, H. Ahn, C. R. Müller and S. Brandani, *International Journal of Greenhouse Gas Control*, 2015, **43**, 198-212.
29. A. Abad, P. Gayán, L. F. de Diego, F. García-Labiano and J. Adánez, *Proceedings of the Combustion Institute*, 2019, **37**, 4361-4369.
30. L. Liu, Z. Li, Z. Li, Y. Larring and N. Cai, *Chemical Engineering Journal*, 2021, **417**.
31. G. Deng, K. Li, Z. Gu, X. Zhu, Y. Wei, X. Cheng and H. Wang, *Chemical Engineering Journal*, 2018, **341**, 588-600.
32. H. Ge, L. Shen, H. Gu and S. Jiang, *Chemical Engineering Journal*, 2015, **262**, 1065-1076.
33. L. Liu, Z. Li, S. Wu, D. Li and N. Cai, *Fuel Processing Technology*, 2021, **213**.
34. S. Lin, Z. Gu, X. Zhu, Y. Wei, Y. Long, K. Yang, F. He, H. Wang and K. Li, *Energy*, 2020, **197**.
35. S. Zhang, H. Gu, J. Zhao, L. Shen and L. Wang, *Energy*, 2019, **186**.

36. M. Rydén and A. Lyngfelt, *International Journal of Hydrogen Energy*, 2006, **31**, 1271-1283.
37. Z. Gu, L. Zhang, C. Lu, S. Qing and K. Li, *Applied Energy*, 2020, **277**.
38. G. Deng, K. Li, G. Zhang, Z. Gu, X. Zhu, Y. Wei and H. Wang, *Applied Energy*, 2019, **253**.
39. J. Bao, Z. Li and N. Cai, *Applied Energy*, 2014, **115**, 549-558.
40. I. Gogolev, T. Pikkarainen, J. Kauppinen, C. Linderholm, B.-M. Steenari and A. Lyngfelt, *Fuel*, 2021, **297**.
41. J. Wang and H. Zhao, *Fuel*, 2016, **165**, 235-243.
42. H. Zhao and J. Wang, *Combustion and Flame*, 2018, **191**, 9-18.
43. Z. Xu, H. Zhao, Y. Wei and C. Zheng, *Combustion and Flame*, 2015, **162**, 3030-3045.
44. J. Bao, Z. Li, H. Sun and N. Cai, *Combustion and Flame*, 2013, **160**, 808-817.
45. X. Zhao, H. Zhou, V. S. Sikarwar, M. Zhao, A.-H. A. Park, P. S. Fennell, L. Shen and L.-S. Fan, *Energy & Environmental Science*, 2017, **10**, 1885-1910.
46. L.-S. Fan, L. Zeng, W. Wang and S. Luo, *Energy & Environmental Science*, 2012, **5**.
47. V. Purnomo, D. Mei, A. H. Soleimanisalim, T. Mattisson and H. Leion, *Energy Fuels*, 2022, **36**, 9768-9779.
48. I. Sampron, L. F. de Diego, F. Garcia-Labiano, M. T. Izquierdo, A. Abad and J. Adanez, *Bioresour Technol*, 2020, **316**, 123908.
49. D. Wang, A. Joshi and L.-S. Fan, *Powder Technology*, 2022, **409**.
50. J. Dai and K. J. Whitty, *Fuel*, 2020, **263**.
51. S. Sundqvist, T. Mattisson, H. Leion and A. Lyngfelt, *Fuel*, 2018, **232**, 693-703.
52. J. Dou, E. Krzystowczyk, X. Wang, T. Robbins, L. Ma, X. Liu and F. Li, *ChemSusChem*, 2020, **13**, 385-393.
53. E. Krzystowczyk, X. Wang, J. Dou, V. Haribal and F. Li, *Phys Chem Chem Phys*, 2020, **22**, 8924-8932.
54. Q. Zheng, M. Lail, S. Zhou and C. C. Chung, *ChemSusChem*, 2019, **12**, 2598-2604.
55. J. Vieten, B. Bulfin, P. Huck, M. Horton, D. Guban, L. Zhu, Y. Lu, K. A. Persson, M. Roeb and C. Sattler, *Energy & Environmental Science*, 2019, **12**, 1369-1384.
56. Z. Sarshar and S. Kaliaguine, *Industrial & Engineering Chemistry Research*, 2013, **52**, 6946-6955.
57. K. Shah, B. Moghtaderi and T. Wall, *Energy & Fuels*, 2012, **26**, 2038-2045.
58. J. Vieten, B. Bulfin, M. Senholdt, M. Roeb, C. Sattler and M. Schmücker, *Solid State Ionics*, 2017, **308**, 149-155.
59. L. Hou, Q. Yu, K. Wang, T. Wang, F. Yang and S. Zhang, *Journal of Thermal Analysis and Calorimetry*, 2018, **137**, 317-325.
60. J. Vieten, B. Bulfin, F. Call, M. Lange, M. Schmücker, A. Francke, M. Roeb and C. Sattler, *Journal of Materials Chemistry A*, 2016, **4**, 13652-13659.
61. D. K. Khosla, S. K. Gupta and D. N. Saraf, *Fuel Processing Technology*, 2007, **88**, 51-63.
62. B. Bulfin, J. Vieten, S. Richter, J. M. Naik, G. R. Patzke, M. Roeb, C. Sattler and A. Steinfeld, *Phys Chem Chem Phys*, 2020, **22**, 2466-2474.
63. I. S. Metcalfe, B. Ray, C. Dejoie, W. Hu, C. de Leeuwe, C. Dueso, F. R. Garcia-Garcia, C. M. Mak, E. I. Papaioannou, C. R. Thompson and J. S. O. Evans, *Nature Chemistry*, 2019, **11**, 638-643.
64. G. Luongo, F. Donat and C. R. Muller, *Phys Chem Chem Phys*, 2020, **22**, 9272-9282.
65. V. Sereda, A. Sednev, D. Tsvetkov and A. Zuev, *Journal of Materials Research*, 2019, **34**, 3288-3295.
66. B. Bulfin, J. Lapp, S. Richter, D. Gubà, J. Vieten, S. Brendelberger, M. Roeb and C. Sattler, *Chemical Engineering Science*, 2019, **203**, 68-75.
67. C.-C. Cormos, *Energy*, 2020, **191**.

68. K. Shah, B. Moghtaderi, J. Zanganeh and T. Wall, *Fuel*, 2013, **107**, 356-370.
69. C. Tian, Q. Fu, Z. Ding, Z. Han and D. Zhang, *Separation and Purification Technology*, 2017, **189**, 54-65.
70. A. Moran and O. Talu, *Industrial & Engineering Chemistry Research*, 2018, **57**, 11981-11987.
71. E. Marek, W. Hu, M. Gaultois, C. P. Grey and S. A. Scott, *Applied Energy*, 2018, **223**, 369-382.
72. B. Sankararao and S. K. Gupta, *Industrial & Engineering Chemistry Research*, 2007, **46**, 3751-3765.
73. L. Jiang, L. T. Biegler and V. G. Fox, *AIChE Journal*, 2003, **49**, 1140-1157.
74. A. V. Nikonov, K. A. Kuterbekov, K. Z. Bekmyrza and N. B. Pavzderin, *Eurasian Journal of Physics and Functional Materials*, 2018, **2**, 274-292.
75. Y. Hao, C.-K. Yang and S. M. Haile, *Chemistry of Materials*, 2014, **26**, 6073-6082.
76. D. de Ligny and P. Richet, *Physical Review B*, 1996, **53**, 3013-3022.
77. H.-C. Wu and Y. S. Lin, *Industrial & Engineering Chemistry Research*, 2017, **56**, 6057-6064.
78. N. Miura, H. Ikeda and A. Tsuchida, *Industrial & Engineering Chemistry Research*, 2016, **55**, 3091-3096.
79. M. Xu, H.-C. Wu, Y. S. Lin and S. Deng, *Chemical Engineering Journal*, 2018, **354**, 62-74.
80. H. Ikeda, S. Nikata, E. Hirakawa, A. Tsuchida and N. Miura, *Chemical Engineering Science*, 2016, **147**, 166-172.
81. Q. Ji, L. Bi, J. Zhang, H. Cao and X. S. Zhao, *Energy & Environmental Science*, 2020, **13**, 1408-1428.
82. Q. Yin, J. Kniep and Y. S. Lin, *Chemical Engineering Science*, 2008, **63**, 5870-5875.
83. Y. Wang, B. Hu, Z. Zhu, H. J. M. Bouwmeester and C. Xia, *J. Mater. Chem. A*, 2014, **2**, 136-143.
84. R. H. Görke, E. J. Marek, F. Donat and S. A. Scott, *International Journal of Greenhouse Gas Control*, 2020, **94**.
85. F. Donat, W. Hu, S. A. Scott and J. S. Dennis, *Industrial & Engineering Chemistry Research*, 2015, **54**, 6713-6723.
86. J. Dou, E. Krzystowczyk, A. Mishra, X. Liu and F. Li, *ACS Sustainable Chemistry & Engineering*, 2018, **6**, 15528-15540.
87. J. Dou, E. Krzystowczyk, X. Wang, A. R. Richard, T. Robbins and F. Li, *Journal of Physics: Energy*, 2020, **2**, 025007.
88. C. Tagliaferri, R. Görke, S. Scott, J. Dennis and P. Lettieri, *Chemical Engineering Research and Design*, 2018, **131**, 686-698.
89. C. Y. Lau, M. T. Dunstan, W. Hu, C. P. Grey and S. A. Scott, *Energy & Environmental Science*, 2017, **10**, 818-831.
90. S. Wang, P. A. W. van der Heide, C. Chavez, A. J. Jacobson and S. B. Adler, *Solid State Ionics*, 2003, **156**, 201-208.
91. J. Yoo, A. Verma, S. Wang and A. J. Jacobson, *Journal of The Electrochemical Society*, 2005, **152**.
92. L. Hou, Q. Yu, T. Wang, K. Wang, Q. Qin and Z. Qi, *Korean Journal of Chemical Engineering*, 2018, **35**, 626-636.
93. B. Bulfin, L. Hoffmann, L. de Oliveira, N. Knoblauch, F. Call, M. Roeb, C. Sattler and M. Schmucker, *Phys Chem Chem Phys*, 2016, **18**, 23147-23154.
94. H. Song, K. Shah, E. Doroodchi, T. Wall and B. Moghtaderi, *Energy & Fuels*, 2013, **28**, 173-182.
95. A. N. Antzaras, E. Heracleous and A. A. Lemonidou, *Fuel Processing Technology*, 2020, **208**, 106513.

96. G. Luongo, F. Donat, A. H. Bork, E. Willinger, A. Landuyt and C. R. Müller, *Advanced Energy Materials*, 2022, **12**, 2200405.
97. W. Ding, K. Zhao, S. Jiang, Z. Zhao, Y. Cao and F. He, *Applied Catalysis A: General*, 2021, **609**, 117910.
98. X. Huang, Z. Yang, J. Qiu, B. Tang, C. Qin, Y. Yan and J. Ran, *Fuel*, 2022, **327**, 125210.
99. Y. Tian, P. R. Westmoreland and F. Li, *Catalysis Today*, 2022, DOI: <https://doi.org/10.1016/j.cattod.2022.04.026>.
100. X. Tian, C. Zheng and H. Zhao, *Applied Catalysis B: Environmental*, 2022, **303**, 120894.
101. W. Sun, G. Zhao, Y. Gao, J. Si, Y. Liu and Y. Lu, *Applied Catalysis B: Environmental*, 2022, **304**, 120948.
102. S. Parishan, P. Littlewood, A. Arinchtein, V. Fleischer and R. Schomäcker, *Catalysis Today*, 2018, **311**, 40-47.
103. J. Huang, K. Zhao, S. Jiang, S. Kang, Y. Lin, Z. Huang, A. Zheng and Z. Zhao, *Fuel Processing Technology*, 2022, **235**, 107352.
104. V. Fleischer, U. Simon, S. Parishan, M. G. Colmenares, O. Görke, A. Gurlo, W. Riedel, L. Thum, J. Schmidt, T. Risse, K.-P. Dinse and R. Schomäcker, *Journal of Catalysis*, 2018, **360**, 102-117.
105. S. Jiang, W. Ding, K. Zhao, Z. Huang, G. Wei, Y. Feng, Y. Lv and F. He, *Fuel*, 2021, **299**, 120932.
106. D. S. Baser, Z. Cheng, J. A. Fan and L.-S. Fan, *ACS Sustainable Chemistry & Engineering*, 2021, **9**, 2651-2660.
107. Z. Cheng, D. S. Baser, S. G. Nadgouda, L. Qin, J. A. Fan and L.-S. Fan, *ACS Energy Letters*, 2018, **3**, 1730-1736.
108. Y. Liu, L. Qin, Z. Cheng, J. W. Goetze, F. Kong, J. A. Fan and L.-S. Fan, *Nature Communications*, 2019, **10**, 5503.
109. M. Tian, C. Wang, Y. Han and X. Wang, *ChemCatChem*, 2021, **13**, 1615-1637.
110. V. Shah, Z. Cheng, P. Mohapatra and L.-S. Fan, *Reaction Chemistry & Engineering*, 2021, **6**, 1928-1939.
111. Y. Kang, M. Tian, C. Huang, J. Lin, B. Hou, X. Pan, L. Li, A. I. Rykov, J. Wang and X. Wang, *ACS Catalysis*, 2019, **9**, 8373-8382.
112. L. Zhang, W. Xu, J. Wu, Y. Hu, C. Huang, Y. Zhu, M. Tian, Y. Kang, X. Pan, Y. Su, J. Wang and X. Wang, *ACS Catalysis*, 2020, **10**, 9420-9430.
113. F. Donat, A. Kierzkowska and C. R. Müller, *Energy & Fuels*, 2022, **36**, 9780-9784.
114. L. Zhang, Y. Hu, W. Xu, C. Huang, Y. Su, M. Tian, Y. Zhu, H. Gong and X. Wang, *Energy & Fuels*, 2020, **34**, 6991-6998.
115. Y. Kang, Y. Han, M. Tian, C. Huang, C. Wang, J. Lin, B. Hou, Y. Su, L. Li, J. Wang and X. Wang, *Applied Catalysis B: Environmental*, 2020, **278**.
116. A. More, C. J. Hansen and G. Vesper, *Catalysis Today*, 2017, **298**, 21-32.
117. V. Shah, Z. Cheng, D. S. Baser, J. A. Fan and L.-S. Fan, *Applied Energy*, 2021, **282**.
118. T. Wang, Y. Gao, Y. Liu, M. Song, J. Liu and Q. Guo, *Fuel*, 2021, **303**, 121286.
119. L. Brody, L. Neal, J. Liu and F. Li, *Energy & Fuels*, 2022, **36**, 9736-9744.
120. L. Brody, L. Neal, V. Haribal and F. Li, *Chemical Engineering Journal*, 2021, **417**.
121. S. Yusuf, L. Neal, Z. Bao, Z. Wu and F. Li, *ACS Catalysis*, 2019, **9**, 3174-3186.
122. L. Neal, A. Shafiearhood and F. Li, *Applied Energy*, 2015, **157**, 391-398.
123. Y. Ni, C. Wang, Y. Chen, X. Cai, B. Dou, H. Chen, Y. Xu, B. Jiang and K. Wang, *Applied Thermal Engineering*, 2017, **124**, 454-465.
124. J. Y. Kim, N. Ellis, C. J. Lim and J. R. Grace, *Fuel*, 2020, **271**, 117665.
125. Y. Han, M. Tian, C. Wang, Y. Kang, L. Kang, Y. Su, C. Huang, T. Zong, J. Lin, B. Hou, X. Pan and X. Wang, *ACS Sustainable Chemistry & Engineering*, 2021, **9**, 17276-17288.

126. C. de Leeuwe, W. Hu, J. Evans, M. von Stosch and I. S. Metcalfe, *Chemical Engineering Journal*, 2021, **423**.
127. A. Hafizi, M. R. Rahimpour and M. Heravi, *International Journal of Hydrogen Energy*, 2019, **44**, 17863-17877.
128. O. Condori, L. F. de Diego, F. Garcia-Labiano, M. T. Izquierdo, A. Abad and J. Adanez, *Energy Fuels*, 2021, **35**, 17182-17196.
129. L. M. Neal, V. P. Haribal and F. Li, *iScience*, 2019, **19**, 894-904.
130. R. Y. Chein and W. H. Hsu, *RENEWABLE ENERGY*, 2020, **153**, 117-129.
131. Q. Lai, T. Cai, S. C. E. Tsang, X. Chen, R. Ye, Z. Xu, M. D. Argyle, D. Ding, Y. Chen, J. Wang, A. G. Russell, Y. Wu, J. Liu and M. Fan, *Science Bulletin*, 2022, DOI: <https://doi.org/10.1016/j.scib.2022.09.013>.
132. R. J. Lee Pereira, P. A. Argyris and V. Spallina, *Applied Energy*, 2020, **280**, 115874.
133. M. M. Sarafraz and F. C. Christo, *Energy Conversion and Management*, 2021, **229**, 113735.
134. W. Gao, J. Guo, P. Wang, Q. Wang, F. Chang, Q. Pei, W. Zhang, L. Liu and P. Chen, *Nature Energy*, 2018, **3**, 1067-1075.
135. X. Tian, C. Zheng, F. Li and H. Zhao, *ACS Sustainable Chemistry & Engineering*, 2021, **9**, 8002-8011.
136. M. S. Sukma, Y. Zheng, P. Hodgson and S. A. Scott, *Energy Fuels*, 2022, **36**, 9410-9422.
137. V. P. Haribal, L. M. Neal and F. Li, *Energy*, 2017, **119**, 1024-1035.
138. X. Zhu, Q. Imtiaz, F. Donat, C. R. Müller and F. Li, *Energy & Environmental Science*, 2020, **13**, 772-804.
139. S. Bhavsar and G. Vesper, *RSC Adv.*, 2014, **4**, 47254-47267.
140. Y. Zhang, F. Kong, A. Tong and L.-S. Fan, *Industrial & Engineering Chemistry Research*, 2020, **59**, 5877-5890.
141. D. Li, R. Xu, X. Li, Z. Li, X. Zhu and K. Li, *Energy & Fuels*, 2020, **34**, 5381-5413.
142. S. Bhavsar, M. Najera, R. Solunke and G. Vesper, *Catalysis Today*, 2014, **228**, 96-105.
143. L. M. Neal, S. Yusuf, J. A. Sofranko and F. Li, *Energy Technology*, 2016, **4**, 1200-1208.
144. R. B. Dudek and F. Li, *Fuel Processing Technology*, 2021, **218**.
145. V. P. Haribal, Y. Chen, L. Neal and F. X. Li, *Engineering-Proc*, 2018, **4**, 714-721.
146. M. Badlani and I. E. Wachs, *Catalysis Letters*, 2001, **75**, 137-149.
147. S. Yusuf, L. M. Neal and F. Li, *ACS Catalysis*, 2017, **7**, 5163-5173.
148. L. Zeng, Z. Cheng, J. A. Fan, L.-S. Fan and J. Gong, *Nature Reviews Chemistry*, 2018, **2**, 349-364.
149. A. Joshi, V. Shah, P. Mohapatra, S. Kumar, R. K. Joshi, M. Kathe, L. Qin, A. Tong and L.-S. Fan, *Advances in Applied Energy*, 2021, **3**.
150. S. Chen, C. Pei, X. Chang, Z. J. Zhao, R. Mu, Y. Xu and J. Gong, *Angew Chem Int Ed Engl*, 2020, **59**, 22072-22079.
151. L. M. Neal, A. Shafieifarhood and F. Li, *ACS Catalysis*, 2014, **4**, 3560-3569.
152. A. Shafieifarhood, J. C. Hamill, L. M. Neal and F. Li, *Phys Chem Chem Phys*, 2015, **17**, 31297-31307.
153. S. Yusuf, V. Haribal, D. Jackson, L. Neal and F. Li, *Applied Catalysis B: Environmental*, 2019, **257**.
154. S. Yusuf, L. Neal, V. Haribal, M. Baldwin, H. H. Lamb and F. Li, *Applied Catalysis B: Environmental*, 2018, **232**, 77-85.
155. Y. Gao, X. Wang, N. Corolla, T. Eldred, A. Bose, W. Gao and F. Li, *Sci Adv*, 2022, **8**, eabo7343.
156. Y. Gao, X. Wang, J. Liu, C. Huang, K. Zhao, Z. Zhao, X. Wang and F. Li, *Sci Adv*, 2020, **6**, eaaz9339.

157. F. Hao, Y. Gao, J. Liu, R. Dudek, L. Neal, S. Wang, P. Liu and F. Li, *Chemical Engineering Journal*, 2021, **409**.
158. F. Hao, Y. Gao, L. Neal, R. B. Dudek, W. Li, C. Chung, B. Guan, P. Liu, X. Liu and F. Li, *Journal of Catalysis*, 2020, **385**, 213-223.
159. R. B. Dudek, X. Tian, M. Blivin, L. M. Neal, H. Zhao and F. Li, *Applied Catalysis B: Environmental*, 2019, **246**, 30-40.
160. X. Tian, R. B. Dudek, Y. Gao, H. Zhao and F. Li, *Catalysis Science & Technology*, 2019, **9**, 2211-2220.
161. X. Zhu, Y. Gao, X. Wang, V. Haribal, J. Liu, L. M. Neal, Z. Bao, Z. Wu, H. Wang and F. Li, *Nat Commun*, 2021, **12**, 1329.
162. R. B. Dudek, X. Tian, M. Blivin, L. M. Neal, H. B. Zhao and F. X. Li, *Appl Catal B-Environ*, 2019, **246**, 30-40.
163. S. Yusuf, L. M. Neal, V. P. Haribal, M. Baldwin, H. H. Lamb and F. Li, *Applied Catalysis B: Environmental*, 2018, **232**, 77-85.
164. J. Liu, S. Yusuf, D. Jackson, W. Martin, D. Chacko, K. Vogt-Lowell, L. Neal and F. Li, *Applied Catalysis A: General*, 2022, **646**, 118869.
165. P. H. Bottelberghs, E. Everts and G. H. J. Broers, *Materials Research Bulletin*, 1976, **11**, 263-267.
166. X. Ji, Y. Liu, J. Liu and J. Zhang, *Applied Catalysis B: Environmental*, 2022, **307**, 121194.
167. Y. Gao, X. Wang, J. Liu, C. Huang, K. Zhao, Z. Zhao, X. Wang and F. Li, *Science Advances*, **6**, eaaz9339.
168. Y. Gao, X. Wang, N. Corolla, T. Eldred, A. Bose, W. Gao and F. Li, *Science Advances*, **8**, eabo7343.
169. M. Cassir, G. Moutiers and J. Devynck, *Journal of The Electrochemical Society*, 2019, **140**, 3114-3123.
170. M. Muhler, J. Schütze, M. Wesemann, T. Rayment, A. Dent, R. Schlögl and G. Ertl, *Journal of Catalysis*, 1990, **126**, 339-360.
171. T. Hirano, *Applied Catalysis*, 1986, **26**, 65-79.
172. O. Shekhah, W. Ranke and R. Schlögl, *Journal of Catalysis*, 2004, **225**, 56-68.
173. Y. Gao, S. Wang, F. Hao, Z. Dai and F. Li, *ACS Sustainable Chemistry & Engineering*, 2020, **8**, 14268-14273.
174. N. K. Razdan and A. Bhan, *Journal of Catalysis*, 2020, **389**, 667-676.
175. L. Y. Chen, L. W. Lin, Z. S. Xu, X. S. Li and T. Zhang, *Journal of Catalysis*, 1995, **157**, 190-200.
176. M. Rahman, A. Sridhar and S. J. Khatib, *Applied Catalysis A: General*, 2018, **558**, 67-80.
177. P. Mériaudeau, L. V. Tiep, V. T. T. Ha, C. Naccache and G. Szabo, *Journal of Molecular Catalysis A: Chemical*, 1999, **144**, 469-471.
178. D. Wang, J. H. Lunsford and M. P. Rosynek, *Topics in Catalysis*, 1996, **3**, 289-297.
179. R. W. Borry, Y. H. Kim, A. Huffsmith, J. A. Reimer and E. Iglesia, *The Journal of Physical Chemistry B*, 1999, **103**, 5787-5796.
180. Y. Xu, W. Liu, S.-T. Wong, L. Wang and X. Guo, *Catalysis Letters*, 1996, **40**, 207-214.
181. L. Wang, L. Tao, M. Xie, G. Xu, J. Huang and Y. Xu, *Catalysis Letters*, 1993, **21**, 35-41.
182. X. Wang, Y. Gao, E. Krzystowczyk, S. Iftikhar, J. Dou, R. Cai, H. Wang, C. Ruan, S. Ye and F. Li, *Energy & Environmental Science*, 2022, **15**, 1512-1528.
183. J. Fan, W. Li, S. Li and J. Yang, *Adv Sci (Weinh)*, 2022, **9**, e2202811.
184. N. R. Singstock, C. J. Bartel, A. M. Holder and C. B. Musgrave, *Advanced Energy Materials*, 2020, **10**.

185. X. Zhang, C. Pei, X. Chang, S. Chen, R. Liu, Z. J. Zhao, R. Mu and J. Gong, *J Am Chem Soc*, 2020, **142**, 11540-11549.
186. D. Kang, H. S. Lim, M. Lee and J. W. Lee, *Applied Energy*, 2018, **211**, 174-186.
187. M. Hye Jeong, D. Hyung Lee, J. Won Moon, J. Sun, J. Soon Choi, D. Sik Hong, C.-H. Chung and J. Wook Bae, *Chemical Engineering Journal*, 2022, **433**, 134621.
188. S. Chen, L. Zeng, R. Mu, C. Xiong, Z.-J. Zhao, C. Zhao, C. Pei, L. Peng, J. Luo, L.-S. Fan and J. Gong, *Journal of the American Chemical Society*, 2019, **141**, 18653-18657.
189. H. Yan, W. Gao, Q. Wang, Y. Guan, S. Feng, H. Wu, Q. Guo, H. Cao, J. Guo and P. Chen, *The Journal of Physical Chemistry C*, 2021, **125**, 6716-6722.
190. C. Xiong, Y. Wu, M. Feng, J. Fang, D. Liu, L. Shen, M. D. Argyle, K. A. M. Gasem and M. Fan, *Applied Energy*, 2022, **323**, 119519.
191. D. F. Swearer, N. R. Knowles, H. O. Everitt and N. J. Halas, *ACS Energy Letters*, 2019, **4**, 1505-1512.
192. C. Ruan, X. Wang, C. Wang, L. Zheng, L. Li, J. Lin, X. Liu, F. Li and X. Wang, *Nature Communications*, 2022, **13**, 718.
193. Q. Yang, M. Yan, L. Zhang, X. Xia, Y. Zhu, C. Zhang, B. Zhao, X. Ma and X. Wang, *Energy Conversion and Management*, 2021, **231**, 113845.
194. I. S. Metcalfe, B. Ray, C. Dejoie, W. Hu, C. de Leeuwe, C. Dueso, F. R. Garcia-Garcia, C. M. Mak, E. I. Papaioannou, C. R. Thompson and J. S. O. Evans, *Nat Chem*, 2019, **11**, 638-643.
195. K. Kousi, D. Neagu, L. Bekris, E. Cali, G. Kerherve, E. I. Papaioannou, D. J. Payne and I. S. Metcalfe, *Journal of Materials Chemistry A*, 2020, **8**, 12406-12417.
196. R. Liu, C. Pei, X. Zhang, S. Chen, H. Li, L. Zeng, R. Mu and J. Gong, *Chinese Journal of Catalysis*, 2020, **41**, 1140-1151.
197. Y. Q. Xu, B. W. Lu, C. Luo, J. Chen, Z. W. Zhang and L. Q. Zhang, *CHEMICAL ENGINEERING JOURNAL*, 2021, **406**.
198. C. Dang, Z. Li, J. Long, W. Yang and W. Cai, *Fuel*, 2022, **324**, 124468.
199. L. C. Buelens, V. V. Galvita, H. Poelman, C. Detavernier and G. B. Marin, *Science*, 2016, **354**, 449-452.
200. T. Xu, X. Wang, B. Xiao, H. Zhao and W. Liu, *Fuel Processing Technology*, 2022, **228**, 107169.
201. V. P. Haribal, F. He, A. Mishra and F. Li, *ChemSusChem*, 2017, **10**, 3402-3408.
202. A. Mishra, A. Shafiefarhood, J. Dou and F. Li, *Catalysis Today*, 2020, **350**, 149-155.
203. S. Iftikhar, W. Martin, Y. Gao, X. Yu, I. Wang, Z. Wu and F. Li, *Catalysis Today*, 2022, DOI: <https://doi.org/10.1016/j.cattod.2022.07.022>.
204. H. S. Lim, M. Kim, Y. Kim, H. S. Kim, D. Kang, M. Lee, A. Jo and J. W. Lee, *ACS Applied Energy Materials*, 2022, **5**, 8437-8442.
205. M. Lee, H. S. Lim, Y. Kim and J. W. Lee, *Energy Conversion and Management*, 2020, **207**, 112507.
206. V. Singh, L. C. Buelens, H. Poelman, M. Saeys, G. B. Marin and V. V. Galvita, *Journal of CO2 Utilization*, 2022, **61**, 102014.
207. B. Jin, N. V. Srinath, H. Poelman, C. Detavernier, Z. Liang, G. B. Marin and V. V. Galvita, *AIChE Journal*, 2022, **68**.
208. A. Longo, S. A. Theofanidis, H. Poelman, D. Banerjee, G. B. Marin and V. V. Galvita, *ChemCatChem*, 2022, **14**.
209. H. Gu, Y. Gao, S. Iftikhar and F. Li, *Journal of Materials Chemistry A*, 2022, **10**, 3077-3085.
210. L. Brody, R. Cai, A. Thornton, J. Liu, H. Yu and F. Li, *ACS Sustainable Chemistry & Engineering*, 2022.
211. R. Chang, X. Wu, O. Cheung and W. Liu, *Journal of Materials Chemistry A*, 2022, **10**, 1682-1705.

212. J. Hua, K. Wang, Q. Wang and R. Peng, *Journal of Thermal Analysis and Calorimetry*, 2021, **146**, 673-680.
213. S. W. Brown, B. Robinson, Y. Wang, C. Wildfire and J. Hu, *Journal of Materials Chemistry A*, 2022, **10**, 15497-15507.
214. R. J. L. Pereira, W. Hu and I. S. Metcalfe, *Energy & Fuels*, 2022, **36**, 9757-9767.
215. J. Liu, Y. Gao, X. Wang and F. Li, *Cell Reports Physical Science*, 2021, **2**, 100503.